



1 **Reconstruction of Climate-Driven Global Terrestrial Water Storage**
2 **Variations (2002–2021)**

3 **Pu Xie, Shuang Yi***

4 National Key Laboratory of Earth System Numerical Modeling and Application,
5 College of Earth and Planetary Sciences, University of Chinese Academy of
6 Sciences, Beijing, 101408, China

7 * Corresponding email: s.yi@ucas.ac.cn

8



9 **Abstract**

10 Terrestrial water storage anomalies (TWSA), jointly influenced by climatic variability and
11 human activities, serve as a key indicator of global climate change. TWSA exhibits pronounced
12 fluctuations across multiple temporal scales, a substantial portion of which can be attributed to
13 climatic variability, such as the El Niño–Southern Oscillation (ENSO). Empirical reconstruction of
14 climate-driven water storage based on relationships between GRACE satellite gravity observations
15 and meteorological forcing data has become a common approach; however, existing models often
16 neglect the regulating role of temperature in the transformation of precipitation into water storage.
17 In this study, we propose a linear, four-parameter coupled recursive model that explicitly
18 incorporates temperature effects on both the conversion and dissipation efficiency of water storage.
19 Using GRACE/GRACE-FO satellite observations and meteorological forcing data, we
20 reconstructed climate-driven TWSA over the global land grid (excluding Antarctica) at a daily
21 temporal resolution and 0.5° spatial resolution for the period 2002 to 2021. For 116 major global
22 river basins, we further derived basin-scale TWSA reconstructions and quantitatively evaluated the
23 fraction of precipitation converted into TWSA. Finally, the reconstructed data were compared with
24 existing reconstruction datasets. Compared with existing reconstruction products, the results
25 indicate that: (1) the proposed method achieves substantially faster parameter convergence,
26 improving computational efficiency by several tens of times during the TWSA reconstruction
27 process; (2) the proposed model demonstrates superior performance in approximately 89% of river
28 basins and 62% of global land grid cells. Specifically, the Nash–Sutcliffe efficiency (NSE) exceeds
29 0.7 in 84 out of 116 basins, and 62% of global land grids exhibit NSE values greater than 0. This
30 study enhances the understanding of the mechanisms governing terrestrial water storage variations
31 at both global and regional scales, provides a quantitative assessment of climate-driven water
32 storage changes, and offers a solid foundation for disentangling the respective impacts of climatic
33 variability and human activities on water resources.

34 **Keywords: GRACE, GRACE-FO, Reconstruction, TWSA, Climate variability**

35



36 **1 Introduction**

37 Terrestrial water storage (TWS) is the total amount of water stored in all components, including
38 surface water (e.g., lakes and reservoirs), groundwater, soil moisture, snow and ice, and vegetation
39 water, and it plays a vital role in the global hydrological cycle. Monitoring TWS is essential not only
40 for understanding the climate system and its variability (Tapley et al., 2019), but also for supporting
41 industrial development and ensuring global food security (Abbott et al., 2019; Rodell et al., 2009;
42 Rodell et al., 2018). Temperature and precipitation are the primary climatic drivers of TWS
43 variations. For instance, precipitation anomalies induced by ENSO are a dominant cause of
44 interannual TWS variability (Liu et al., 2020; Ni et al., 2018).

45 Traditionally, changes in TWS have been estimated using two main approaches. The first is the
46 water balance method, which requires precipitation, evapotranspiration, and runoff data.
47 Precipitation is typically measured by rain gauges, evapotranspiration is monitored using eddy
48 covariance systems (Baldocchi et al., 2001; Pastorello et al., 2020; Ma et al., 2024), and runoff is
49 estimated from discharge records at hydrological gauging stations (Duan et al., 2024). The rate of
50 TWS change ($dTWS/dt$) is then inferred from the water balance Eq. However, because ground-
51 based observation stations are spatially discrete, this method can only provide localized, point-scale
52 information. In regions constrained by limited financial resources or political barriers to data access,
53 the sparse distribution of monitoring sites further hinders the establishment of continuous spatial
54 coverage (Crochemore et al., 2020; Fekete et al., 2012; Laudon et al., 2017). The second is the
55 model-based approach, in which land surface or hydrological models simulate individual storage
56 components such as soil moisture and groundwater, which are then aggregated to estimate total TWS
57 variations. However, both instrumental and measurement errors can propagate through the modeling
58 process, introducing substantial uncertainties into the final TWS estimates (Long et al., 2015;
59 Humphrey et al., 2023). Moreover, the uncertainty associated with hydrological model outputs
60 remains difficult to quantify (Zheng et al., 2023).

61 Since its launch in 2002, the Gravity Recovery and Climate Experiment (GRACE) mission has
62 provided precise measurements of temporal variations in Earth's gravity field and delivered monthly
63 gravity field solutions (Tapley et al., 2019; Chen et al., 2022; Humphrey et al., 2023). Compared
64 with traditional approaches that rely on sparse ground-based observations or hydrological models
65 with large uncertainties, GRACE data have substantially improved the spatial continuity and
66 observational reliability of Earth's gravity measurements, providing a crucial tool for monitoring
67 global water storage changes. A major contributor to temporal variations in the terrestrial gravity
68 field is the variations in TWS, which is jointly driven by natural climate variability, long-term



69 climate change, and human water use (Rodell et al., 2018; An et al., 2021). Distinguishing
70 anthropogenic signals from natural variability in GRACE-observed TWS has therefore become an
71 active research focus (An et al., 2021; Liu et al., 2021; Yi et al., 2016; Zhang et al., 2025).

72 Currently, reconstruction methods for climate-driven TWSA can be broadly classified into two
73 categories. The first category is data-driven approaches, which establish nonlinear mappings
74 between GRACE-based TWSA and climate–hydrological variables using machine learning or
75 neural network models (Fan et al., 2021; Palazzoli et al., 2025; Li et al., 2021; Sun et al., 2020;
76 Zhang et al., 2016; Long et al., 2014; Sun et al., 2021; Yin et al., 2023; Li et al., 2020). The advantage
77 of such approaches lies in their ability to capture complex patterns without requiring prior
78 assumptions about the underlying physical processes (Long et al., 2014) and without being
79 constrained by the spatial resolution of the input drivers. For instance, Zhang et al. (2016)
80 reconstructed TWSA in the Yangtze River Basin for the period from 1979 to 2012 using an artificial
81 neural network driven by precipitation and ERA-Interim soil moisture, and subsequently estimated
82 drought recovery times. Sun et al. (2021) introduced an automated machine learning framework for
83 GRACE-based TWSA reconstruction, integrating GLDAS model outputs together with
84 meteorological and climatic predictors to combine physical constraints with data-driven learning.
85 Palazzoli et al. (2025) developed unidirectional and bidirectional Long Short-Term Memory
86 networks to construct four climate-driven models, generating a continuous global TWSA record at
87 0.5° resolution for the period from 1984 to 2021. Li et al. (2021) combined statistical analysis, time
88 series decomposition, and machine learning techniques to reconstruct global (excluding Antarctica)
89 gridded TWSA for the period from 1979 to 2020 using multiple predictors, such as sea surface
90 temperature and climate indices. Yin et al. (2023) also adopted this approach and incorporated a
91 broader range of predictors in addition to conventional climatic variables, including land use data
92 and vegetation indices, to reconstruct a continuous global monthly TWSA dataset at 0.5° spatial
93 resolution for the period 1940 to 2022.

94 The second category of methods involves data-driven statistical models for reconstructing
95 TWSA (Zhong et al., 2019; Zhong et al., 2025; Humphrey and Gudmundsson, 2019; Xiao et al.,
96 2025). Humphrey and Gudmundsson (2019) proposed a statistical reconstruction approach that uses
97 only precipitation and temperature as predictors to estimate climate-driven TWS at both daily and
98 monthly time scales over the past century. Their method not only successfully filled the ~1-year
99 observational gap between the GRACE and GRACE-FO missions but also demonstrated
100 performance comparable to or exceeding that of several global hydrological models. However, their
101 model incorporates a mathematical fitting procedure to align the reconstructed TWSA with GRACE



102 observations. This adjustment improves amplitude consistency but does not provide a clear physical
103 interpretation. Building on this framework, Zhong et al. (2025) introduced a key modification by
104 incorporating the concept of the “mean daily fraction of precipitation converted to TWS”, thereby
105 adding a physically interpretable representation of the precipitation-to-storage transformation
106 process. Based on this enhancement, they re-estimated that approximately 64% of terrestrial
107 precipitation contributed to TWS across 121 global river basins during the period from 2002 to 2021,
108 with substantial spatial variability linked to climatic and geographic conditions. The specific
109 formulations and reconstruction workflows of both statistical models are detailed in Sections 3.1
110 and 3.2 of this study.

111 Expanding upon the frameworks of Humphrey and Gudmundsson (2019) and Zhong et al.
112 (2025), this study further advances parameter design. Whereas previous models relied on two
113 empirical parameters without clear physical meaning, we propose a linear, four-parameter coupled
114 recursive model at the daily time scale. This model explicitly incorporates temperature modulation
115 of the immediate infiltration efficiency of precipitation, as well as the retention rate of water storage
116 and its temperature sensitivity. The model includes four parameters, all of which have clear physical
117 interpretation. In addition, the approach has been optimized for computational efficiency and
118 numerical stability. Using this method, we reconstructed a global (excluding Antarctica) gridded
119 TWSA dataset at 0.5° spatial resolution and monthly time step for the period from 2002 to 2021
120 (the product name is provided in Section 4.1). The reconstructed TWSA closely matches GRACE
121 observations and achieves accuracy levels comparable to or exceeding those of existing
122 reconstruction products, as demonstrated in comprehensive benchmark evaluations.

123

124 **2 Data**

125 **Table 1 List of the data sets**

Dataset	Time	Spatial resolution	Temporal resolution
GSFC RL06v2.0 mascon solution	2002—2021	1°equal area (provided on 0.5°)	monthly
JPL CRI Filtered RL06.1v03 mascon solution	2002—2021	3.0°equal area (provided on 0.5°)	monthly



Precipitation (ERA5-land)	2000—2025	0.1°	hourly
Precipitation (MSWEP v2.8)	2000—2021	0.1°	daily
Temperature (ERA5-land)	2000—2025	0.1°	hourly
Temperature (GLDAS v2.2)	2003—2021	0.25°	daily
Evapotranspiration (ERA5-land)	2000—2020	0.1°	hourly
GRACE-REC (Humphrey’s reconstruction)	2002—2019	0.5°	monthly

126

127 **2.1 GRACE data**

128 This study employs two GRACE/GRACE-FO mascon solutions (Table 1): the JPL RL06 v03
129 mascon product (JPLM) provided by the Jet Propulsion Laboratory (Wiese et al., 2019), and the
130 GSFC RL06v2.0 mascon product (GSFCM) provided by the NASA Goddard Space Flight Center
131 (Loomis et al., 2019). All datasets cover the period from 2002 to 2021. The native resolution of
132 JPLM is $3^\circ \times 3^\circ$ equal-area caps, and the data are distributed on a 0.5° latitude and longitude grid.
133 The GSFCM product has a native resolution of $1^\circ \times 1^\circ$ equal-area caps and is also provided on a
134 0.5° grid. Both mascon products have been preprocessed with geocenter correction, degree-2
135 replacement, and GIA correction, and thus require no further post-processing (Lan and Wenke,
136 2022).

137 **2.2 Precipitation and Temperature Data**

138 This study employs two precipitation products and two temperature products (Table 1). For
139 precipitation, the following datasets are used: (1) The ERA5-Land dataset, developed by the
140 European Centre for Medium-Range Weather Forecasts (ECMWF), is the land component of the
141 ERA5 reanalysis. It is driven by atmospheric forcing variables from ERA5 and provides hourly
142 precipitation data at a spatial resolution of $0.1^\circ \times 0.1^\circ$ (~9 km), covering the period from January
143 1950 to present (Muñoz-Sabater et al., 2021; Muñoz Sabater, 2019); (2) The Multi-Source
144 Weighted-Ensemble Precipitation (MSWEP) version 2.8 dataset (Beck et al., 2017; Beck et al., 2019)
145 spans from 1979 to present and offers precipitation estimates at $0.1^\circ \times 0.1^\circ$ spatial resolution and



146 multiple temporal resolutions (3-hourly, daily, and monthly). In this study, the daily product is used.
147 MSWEP combines gauge observations, satellite retrievals, and reanalysis data using a weighted
148 ensemble approach to provide high-accuracy global precipitation estimates (Beck et al., 2017).

149 For temperature, the following datasets are used: (1) The ERA5-Land reanalysis dataset
150 produced by ECMWF (Muñoz Sabater, 2019); (2) NASA's Global Land Data Assimilation System
151 (GLDAS) developed the GLDAS v2.2 Catchment Land Surface Model (CLSM) product (Li et al.,
152 2019). This model offers a physically based framework suitable for assimilating GRACE-derived
153 TWS observations. The GLDAS v2.2 dataset includes both a main version and an early product.
154 This study uses the main version, which spans from February 2003 to July 2025 (as of manuscript
155 preparation), with a spatial resolution of $0.25^\circ \times 0.25^\circ$ and a daily temporal resolution.

156 ERA5-Land precipitation and temperature are used as the primary meteorological inputs in this
157 study. The MSWEP precipitation and GLDAS temperature datasets are additionally used to compare
158 standard deviations with ERA5-Land, in order to assess the uncertainty of ERA5-Land forcing data
159 and support the subsequent parameter uncertainty analysis.

160 **2.3 Ancillary Data**

161 This study selected 116 river basins, with basin boundaries obtained from the Global Runoff
162 Data Centre (GRDC). The classification of basin climate types was based on the mean annual aridity
163 index, derived from the Global Aridity Index and Potential Evapotranspiration Climate Database
164 (Zomer et al., 2022; Trabucco and Zomer, 2019), which is available in GeoTIFF format. The aridity
165 index is defined as the ratio of annual precipitation to mean annual potential evapotranspiration,
166 where higher values indicate more humid conditions. Climate types were categorized according to
167 the aridity index as follows: arid (aridity index < 0.2), semi-arid ($0.2 \leq$ aridity index < 0.5),
168 semi-humid ($0.5 \leq$ aridity index < 0.65), and humid (aridity index ≥ 0.65).

169

170 **3 Methods**

171 **3.1 Previous Statistical Models for TWSA Reconstruction**

172 **3.1.1 Humphrey's Reconstruction Model**

173 Precipitation is the primary input to terrestrial water storage. Statistical models that reconstruct
174 TWSA from daily precipitation and temperature can be used to quantify the influence of climatic
175 variability on terrestrial water storage (Humphrey and Gudmundsson, 2019). For comparison



176 purposes, we first revisit the statistical reconstruction model proposed by Humphrey and
177 Gudmundsson (2019) :

$$178 \quad TWS(t) = TWS(t-1) \cdot e^{-\frac{1}{\tau(t)}} + P(t), \quad (1)$$

179 where t is the daily time index, $TWS(t)$ is the water storage on day t , $P(t)$ is the
180 precipitation input on day t , and $\tau(t)$ is the water residence time. A larger τ implies slower losses
181 through evapotranspiration or runoff, while a smaller τ indicates faster depletion.

182 $\tau(t)$ is defined as a function of temperature to represent the seasonal variations in water
183 residence time.

$$184 \quad \tau(t) = a + b \cdot T_z(t), \quad (2)$$

185 where a and b are model parameters to be calibrated.

186 To reduce the influence of extreme temperatures on model stability, the original temperature
187 $T(t)$ is first detrended and standardized, then transformed using a sigmoid function:

$$188 \quad T_z = 1 - \tanh\left(\frac{T_0 - \text{mean}(T_0)}{\text{SD}(T_0)}\right). \quad (3)$$

189 Since subzero temperatures have negligible effects on residence time (as temperature changes
190 exert little influence on storage losses such as evapotranspiration and runoff under freezing or
191 insufficient thawing conditions), the original temperature series $T(t)$ was preprocessed as follows:

$$192 \quad T_0 = \begin{cases} 0, & T < 0 \\ T, & T \geq 0 \end{cases}. \quad (4)$$

193 The initial water storage $TWS(0)$ is computed as the ratio of long-term mean precipitation to
194 mean water loss rate:

$$195 \quad TWS(0) = \frac{\text{mean}(P)}{1 - \text{mean}\left(e^{-\frac{1}{\tau(t)}}\right)}. \quad (5)$$

196 The daily TWS series is aggregated to monthly means $TWS(t_m)$ and calibrated against
197 deseasonalized and detrended GRACE TWSA at the monthly scale. The model parameters
198 a , b and β are calibrated using a Markov Chain Monte Carlo (MCMC) approach, with the objective
199 of minimizing the sum of squared residuals between the simulated and GRACE-derived TWSA:

$$200 \quad \text{anom}(GRACE(t_m)) = \beta \cdot \text{anom}(TWS(t_m)) + \epsilon. \quad (6)$$

201 The coefficient β serves as a scaling factor obtained from MCMC calibration, ϵ denotes the
202 residual term, and $\text{anom}(\cdot)$ represents the anomaly series after removal of the seasonal cycle and
203 linear trend.



204 3.1.2 Zhong's Reconstruction Model

205 The scaling factor β in Eq. (6) lacks clear physical meaning and serves merely as a calibration
206 parameter, resulting in a strong dependence of the reconstruction on GRACE observations. Building
207 on this framework, Zhong et al. (2025) proposed an improved formulation for reconstructing
208 terrestrial water storage :

$$209 \quad TWS(t) = TWS(t-1) \cdot e^{-\frac{1}{\tau(t)}} + \beta \cdot P(t). \quad (7)$$

210 In this formulation, the parameter β has a clear physical interpretation, representing the mean
211 fraction of daily precipitation that contributes to water storage. The residence time $\tau(t)$ is defined
212 as in Eq. (2). It is important to note that this β is fundamentally different from the scale factor used
213 in Eq. (6).

214 The daily TWS series is aggregated to monthly means $TWS(t_m)$ and calibrated against
215 deseasonalized and detrended GRACE TWSA at the monthly scale. The model parameters
216 a, b and β are also calibrated using the MCMC approach:

$$217 \quad anom(Grace(t_m)) = anom(TWS(t_m)) + \epsilon. \quad (8)$$

218 Owing to the high nonlinearity of the estimation model, parameter optimization is prone to
219 being trapped in local optima. To reduce the bias caused by incomplete chain convergence, the
220 MCMC calibration was repeated 50 times for each basin. All parameter sets falling within the $\pm 1 \cdot$
221 σ range were retained, and their averages were taken as the final estimates of parameters a, b and β .
222 The standard deviation of these filtered parameters was then calculated to represent the inter-basin
223 uncertainty of β .

224 3.2 Proposed Reconstruction Method

225 3.2.1 Model formulation

226 The two preceding approaches describe the residence time (Eq. 2) as a temperature-dependent
227 function. However, the parameters a and b in its definition are merely calibration coefficients
228 without explicit physical meaning when substituted into the exponential decay function (Eq. 1 and
229 7). In this study, we propose a linearized modification of the water storage reconstruction formula,
230 which simultaneously accounts for the temperature-regulated memory term $TWS(t-1)$, and the
231 temperature-dependent precipitation conversion rate, as follows:

$$232 \quad TWS(t) = (a \cdot T_z + b) \cdot P(t) + (c \cdot T_z + d) \cdot TWS(t-1). \quad (9)$$

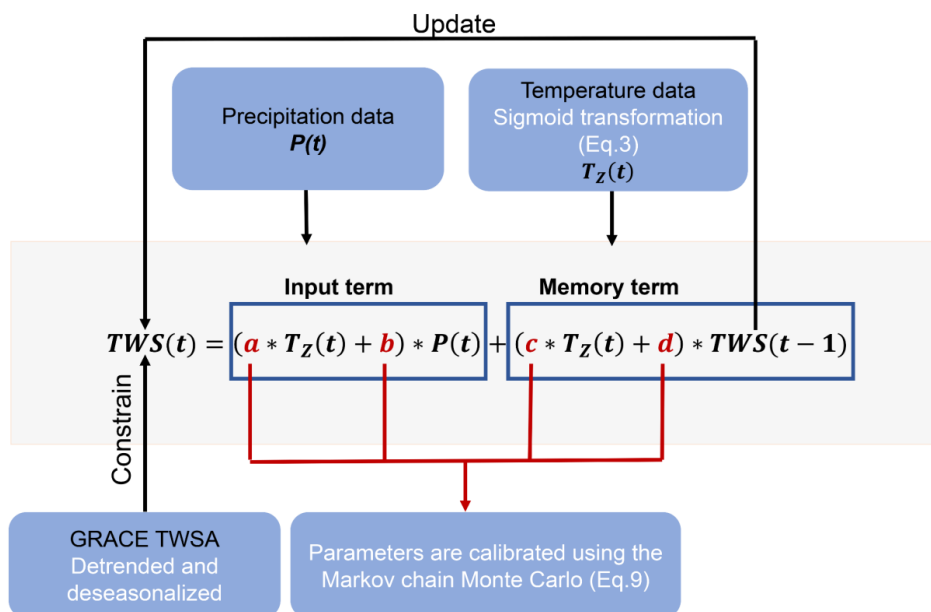
233 All four parameters in the Eq. are endowed with clear physical interpretations. Specifically,
234 parameter a reflects the regulating effect of temperature on the conversion of precipitation into



235 water storage. Parameter b represents the proportion of precipitation that directly contributes to
 236 TWS when $T_z = 0$. Parameter c quantifies the temperature-mediated influence of antecedent
 237 water storage $TWS(t - 1)$ on current storage $TWS(t)$. Parameter d represents the proportion of
 238 storage retained from the previous time step that is independent of temperature variations.

239 When solving Eq. (1), (7), and (9), it is necessary to specify the initial water storage value,
 240 $TWS(0)$. Humphrey and Gudmundsson (2019) and Zhong et al. (2025) assumed that the initial water
 241 storage corresponds to an equilibrium state, as defined in Eq. (5). Although using Eq. (5) provides
 242 a unique and reproducible starting condition, it inherently assumes that water storage is close to
 243 equilibrium at the beginning of the reconstruction period. However, if a basin experiences an
 244 extreme hydroclimatic condition at the initial time step, adopting Eq. (5) may introduce systematic
 245 biases and consequently affect the MCMC calibration of other parameters. In this study, $TWS(0)$
 246 is also treated as a variable and is simultaneously estimated together with other model parameters
 247 through a joint least-squares and MCMC optimization. This approach eliminates the need to assume
 248 equilibrium conditions at the start of the reconstruction period and is therefore more suitable for
 249 basins under nonequilibrium states, such as those influenced by prolonged droughts or intensive
 250 groundwater extraction (see Section 5.1.2 for details).

251 The calibration procedure in this section follows exactly the same steps as described in Section
 252 3.1.2, with Eq. (8) retained throughout the process. The reconstruction logic of TWSA is illustrated
 253 in Fig. 1.



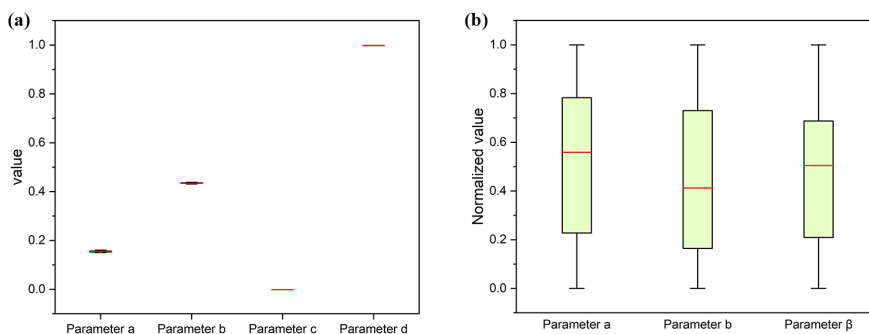


255 Figure 1: Illustration of the physical meaning of parameters.

256 Compared with the methods of Humphrey and Gudmundsson (2019) and Zhong et al. (2025),
257 this study linearizes the memory term $TWS(t-1) \cdot e^{-\frac{1}{\tau(t)}}$ as $(c \cdot T_z + d) \cdot TWS(t-1)$. A key
258 advantage of this linearization is its computational stability and rapid convergence, which
259 substantially improves inversion efficiency. Under the same parameter calibration framework as
260 Zhong et al. (2025), both our model and the Zhong's model were run with 50 independent MCMC
261 chains for the Yellow River to derive the posterior parameter distributions. The parameter dispersion
262 (indicated by the box height) in our model (Fig. 2a) is considerably narrower than that in Zhong's
263 model (Fig. 2b), indicating that our model exhibits smaller parameter uncertainties and faster chain
264 convergence. Consequently, a single MCMC calibration is sufficient for each basin in our method,
265 greatly reducing computation time without a noticeable loss of fitting accuracy. Specifically, on our
266 computing platform (Intel 13th Gen Core i9-13900H processor, 14 cores, base frequency 2.60 GHz,
267 turbo frequency up to ~5.4 GHz, and 16 GB RAM), the Zhong's model required 50 parameter
268 calibrations, taking a total of 353.8 s for a single basin, whereas our method required only one
269 calibration, completing the computation in 6.8 s.

270 In summary, this study improves upon previous models in three aspects:

- 271 (1) Linearization of the memory term. The linearization not only accelerates computational
272 performance but also enhances the physical interpretability of parameters.
273 (2) Incorporation of the coupling between temperature and precipitation. This mechanism
274 adjusts the fraction of precipitation converted into water storage, leading to a slight
275 improvement in NSE across most basins and substantial enhancement in several cases (see
276 Section 5.2.2).
277 (3) Consideration of the impact of different initial values on model fitting results (see Section
278 5.1.2).



279



280 Figure 2: Comparison of parameter stability in the Yellow River Basin between (a) our reconstruction model and
281 (b) the model of Zhong et al. (2025), based on 50 independent calibrations using the MCMC approach. Parameter
282 medians (red lines) are highlighted.

283 3.2.2 Further interpretation of Our Equations

284 To demonstrate the compatibility of the proposed model with existing approaches, we consider
285 two extreme cases:

286 (1) In the model of Zhong et al. (2025), the memory factor is expressed as $e^{-\frac{1}{\tau(t)}}$. When
287 applying a first-order Taylor expansion to the exponential term in Eq. (7), it can be approximated
288 as:

$$289 \quad TWS(t) = \beta \cdot P(t) + \left(1 - \frac{1}{\tau(t)}\right) \cdot TWS(t-1). \quad (10)$$

290 Our model (Eq. 9) becomes mathematically similar to Eq. (10) when the temperature and
291 precipitation modulation is neglected (i.e., $a = 0$). This indicates that our model degenerates to the
292 first-order linear form of the Zhong model when temperature effects are not considered.

293 (2) Assuming that the memory term is unaffected by temperature ($c = 0$) and exhibits perfect
294 conversion efficiency ($d = 1$), Eq. (9) simplifies to:

$$295 \quad TWSC(t) = TWS(t) - TWS(t-1) = (a \cdot T_z + b) \cdot P(t). \quad (11)$$

296 The water balance Eq. is given as:

$$297 \quad TWSC(t) = P(t) - ET(t) - R(t). \quad (12)$$

298 This implicitly assumes a proportional linear relationship between the loss terms, $ET(t) +$
299 $R(t)$, and the precipitation input $P(t)$: $R(t) + ET(t) = (1 - a \cdot T_z - b) \cdot P(t)$. In other words,
300 the total output is controlled by the input, so even without explicitly representing the loss terms, the
301 Eq. is still able to account for their integrated contribution.

302 3.2.3 Uncertainty Estimation

303 To quantify the uncertainty associated with meteorological forcing data, this study estimates
304 observational errors based on the differences between multiple data sources. Specifically, the
305 standard deviation of daily precipitation differences between ERA5-Land and MSWEP is used as
306 the uncertainty estimate for ERA5-Land precipitation, while the standard deviation of daily
307 temperature differences between ERA5-Land and GLDAS-GLSM is used to estimate the
308 uncertainty in ERA5-Land temperature.

309 Temperature uncertainty:

$$310 \quad \sigma_T = std(T_{ERA5-Land} - T_{GLDAS-GLSM}). \quad (13)$$



311 Precipitation uncertainty:

$$312 \quad \sigma_P = \text{std}(P_{\text{ERA5-Land}} - P_{\text{MSWEP}}). \quad (14)$$

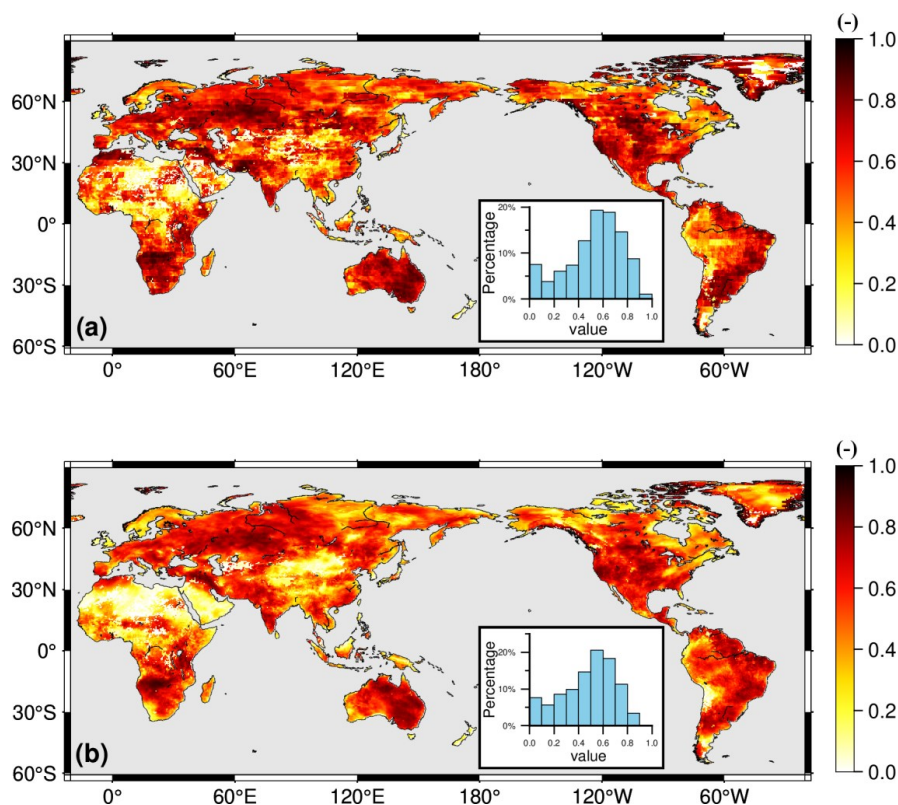
313 Building on this, we adopt a Monte Carlo simulation framework in which Gaussian noise with
314 zero mean and standard deviations of σ_T and σ_P is added to the temperature and precipitation
315 inputs, respectively. For each perturbed dataset, the model is recalibrated to obtain an optimal set of
316 parameters under the given realization. After completing 1,000 simulations, all sets of estimated
317 parameters are collected to derive the uncertainty distributions of both the model parameters and the
318 reconstructed TWS.

319

320 4 Results

321 4.1 Performance summary

322 The performance of the GRACE reconstruction model was evaluated using the NSE. Figure 3
323 presents the spatial distribution of NSE values for 116 major river basins worldwide, and the
324 corresponding numerical results are provided in Table S1. For the reconstruction calibrated against
325 the JPLM product (hereafter referred to as JPL-REC), 53.3% of the 0.5° grid cells exhibited NSE
326 values in the range of 0.5 to 0.8, while 8.6% showed $NSE > 0.8$. High NSE values were primarily
327 concentrated in mid- to high-latitude regions such as North America, Europe, and Australia, where
328 in situ meteorological observations are relatively dense (Fig. 3a). In contrast, regions such as most
329 of Africa and the arid plateau zones of Central Asia showed relatively low NSE values, likely due
330 to the scarcity of precipitation and temperature observations (Xu et al., 2020; Chen et al., 2008). The
331 reconstruction calibrated against the GSFC mascon product (hereafter GSFC-REC) displayed a
332 spatial pattern broadly similar to that of JPL-REC, with 50.2% of grid cells falling within the range
333 from 0.5 to 0.8 and 2.81% exceeding $NSE > 0.8$. The high spatial concordance of NSE between
334 JPL-REC and GSFC-REC indicates that the reconstruction method is largely insensitive to the
335 source of the mascon product, consistent with previous findings (Humphrey and Gudmundsson,
336 2019).



337

338 Figure 3: Spatial distribution of NSE (of de-seasonalized, de-trended anomalies) between our reconstruction and
339 (a) JPLM or (b) GSFCM for the period from 2002 to 2021. Histograms show the distribution of NSE values
340 across all global grid points.

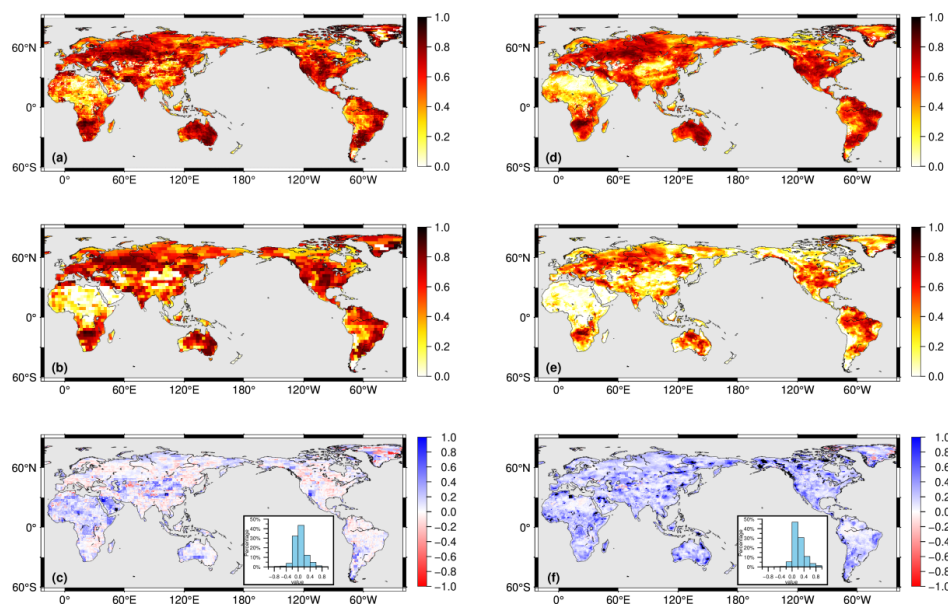
341 4.2 Comparisons

342 4.2.1 Comparison with the Humphrey's Model

343 At the grid scale, we first compared the reconstruction results from this study (JPL-REC and
344 GSFC-REC) with those of Humphrey and Gudmundsson (2019), which were trained using the
345 JPLM and GSFCM products, respectively (hereafter referred to as Humphrey-JPL-REC and
346 Humphrey-GSFC-REC). Figure 4 presents the spatial distribution of NSE values between the
347 reconstructed and GRACE-derived TWSA after deseasonalization and detrending over the period
348 from 2002 to 2019. Figure 4a and 4d show the NSE performance of JPL-REC and GSFC-REC
349 relative to their corresponding mascon products (JPLM and GSFCM), respectively. Both panels
350 indicate high model performance ($NSE > 0.7$) across large parts of North America, Europe,
351 Australia, and southern Africa, whereas low NSE values ($NSE < 0.4$) are evident in parts of North



352 Africa, Central Asia, and the Arabian Peninsula. Figure 4b and 4e show the NSE performance of
353 Humphrey-JPL-REC and Humphrey-GSFC-REC relative to their corresponding mascon products
354 (JPLM and GSFCM), respectively. While the overall spatial patterns are broadly similar to those in
355 Fig. 4a and 4d, the extent of low-performance areas in Africa and Central Asia is noticeably larger
356 in the Humphrey reconstructions. Figure 4c and 4f present the differences in NSE (ΔNSE),
357 calculated as Fig. 4a minus Fig. 4b and Fig. 4d minus Fig. 4e, respectively. Blue shading ($\Delta NSE >$
358 0) indicates regions where the present method outperforms the approach by Humphrey and
359 Gudmundsson (2019). Notably, in Fig. 4c, approximately 63% of the grid cells show $\Delta NSE >$
360 0, with substantial improvements in regions such as the Arabian Peninsula and sub-Saharan Africa,
361 along with scattered enhancements across other continents. Figure 4f demonstrates that under
362 GSFCM constraints, the present method substantially outperforms that of Humphrey and
363 Gudmundsson (2019). One potential explanation lies in the difference in training datasets: while
364 (Humphrey and Gudmundsson, 2019) utilized the GSFC mascon v2.4 (an older version that is no
365 longer publicly available), the present study employs the updated GSFC mascon RL06v2.0. This
366 difference may account for the discrepancies between our results in Fig. 4e and those reported in the
367 original publication by Humphrey and Gudmundsson (2019).



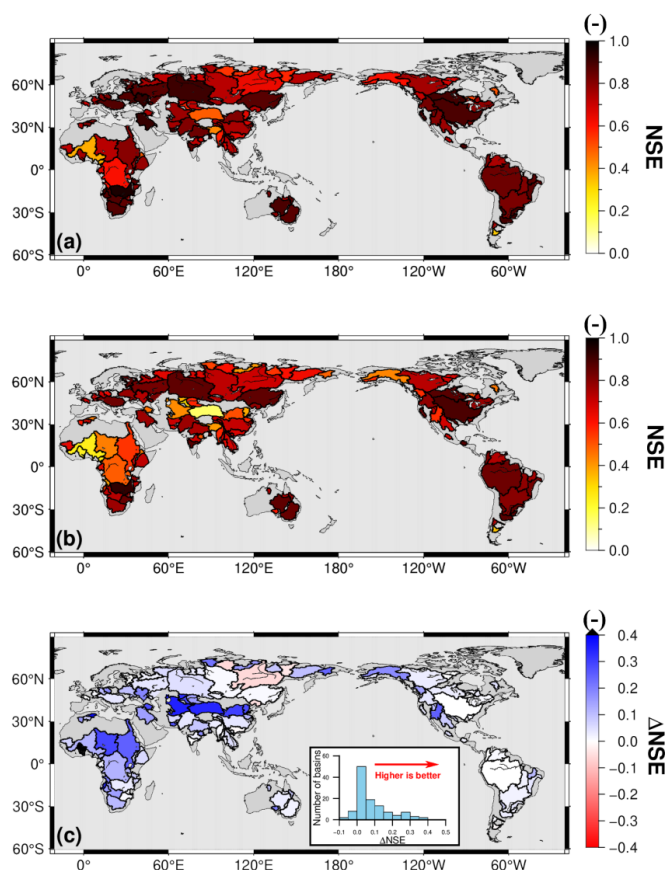
368



369 Figure 4: Spatial distribution of NSE (of de-seasonalized, de-trended anomalies) for the period from 2002 to
370 2019. (a) and (d): NSE of JPL-REC and GSFC-REC against their respective GRACE mascon solutions. (b) and
371 (e): NSE of Humphrey-JPL-REC and Humphrey-GSFC-REC against the corresponding GRACE mascon
372 solutions. (c) and (f): Spatial differences in NSE between our reconstruction and that of Humphrey and
373 Gudmundsson (2019), both relative to the same GRACE mascon solution. Values larger than 0 indicate better
374 performance of our method.

375 4.2.2 Comparison with the Zhong Model

376 We further compared the reconstruction results at the basin scale with those from Zhong et al.
377 (2025). In the comparison across 116 major global river basins, the proposed model achieved a
378 median NSE of 0.76, outperforming the reconstruction by Zhong et al. (2025) (hereafter referred to
379 as Zhong-REC), which had a median NSE of 0.70. Among these basins, 84 (73%) achieved $NSE >$
380 0.7, compared to only 59 (51%) for Zhong-REC. Model performance was closely linked to the
381 quality of the forcing data and the dominant hydrological processes (Yi et al., 2023). Poor
382 performance ($NSE < 0.5$) was observed in basins such as the Congo, Niger, and Sanaga in Africa,
383 and the Tarim River in Central Asia, where sparse ground-based meteorological observations result
384 in large uncertainties in climate forcing data (Xu et al., 2020; Chen et al., 2008). Cold-region basins
385 such as the Yukon, Brahmaputra, Lena, Indigirka, Kolyma, Olenek, Yana, and Khatanga are strongly
386 influenced by glacial and permafrost-driven seasonal accumulation and ablation processes (Riegger
387 and Tourian, 2014; Yi et al., 2023). The linear reservoir assumption fails to adequately capture the
388 mass variations in these basins (Liu et al., 2022), resulting in NSE values ranging from 0.45 to 0.70.
389 In contrast, river basins where hydrological signals are dominant, such as the Amazon, Mississippi,
390 Nelson, and Amur, showed good reconstruction performance with NSE values greater than 0.80.
391 The histogram of ΔNSE (this model minus Zhong-REC) shown in Fig. 5c reveals a positively
392 skewed distribution, indicating performance improvements in the majority of basins. Specifically,
393 37 basins (approximately one-quarter of the sample) exhibited $\Delta NSE > 0.1$. The most pronounced
394 improvements were found in arid and semi-arid regions (Fig. S2), including the Tarim River, Lake
395 Chad, and Yellow River basins. The spatial distribution of regions with the most notable
396 improvements in Fig. 5c closely aligns with the ΔNSE pattern between the proposed model and
397 Humphrey-JPL-REC (Fig. S1), further supporting the role of the coupling between temperature and
398 precipitation and the joint inversion of initial conditions in enhancing reconstruction accuracy in
399 areas with low NSE.



400

401 Figure 5: Spatial distribution of NSE (de-seasonalized, de-trended anomalies) between JPL mascon and two
402 reconstruction models across 116 global river basins for the period 2002 to 2021. The NSE between JPLM and
403 JPL-REC (a); the NSE between JPLM and the reconstruction by Zhong et al. (2025) (b); and their difference
404 ($\Delta NSE = JPL-REC - Zhong-REC$) (c). The inset histogram in (c) illustrates the distribution of ΔNSE across all
405 basins, where positive values indicate better agreement with GRACE observations by our reconstruction model.

406 4.3.3 Comparison of Time Series

407 This section presents a comparison of deseasonalized and detrended monthly TWSA time
408 series across nine representative river basins. Figure 6 illustrates the differences among
409 GRACE/GRACE-FO observations (black line), the present reconstruction (JPL-REC, red line),
410 Zhong-REC (blue line), and Humphrey-JPL-REC (green line) in terms of basin-averaged TWSA
411 time series.

412 Interannual variations in terrestrial water storage are primarily driven by atmospheric
413 circulation anomalies induced by ENSO events, which often trigger hydrological extremes such as

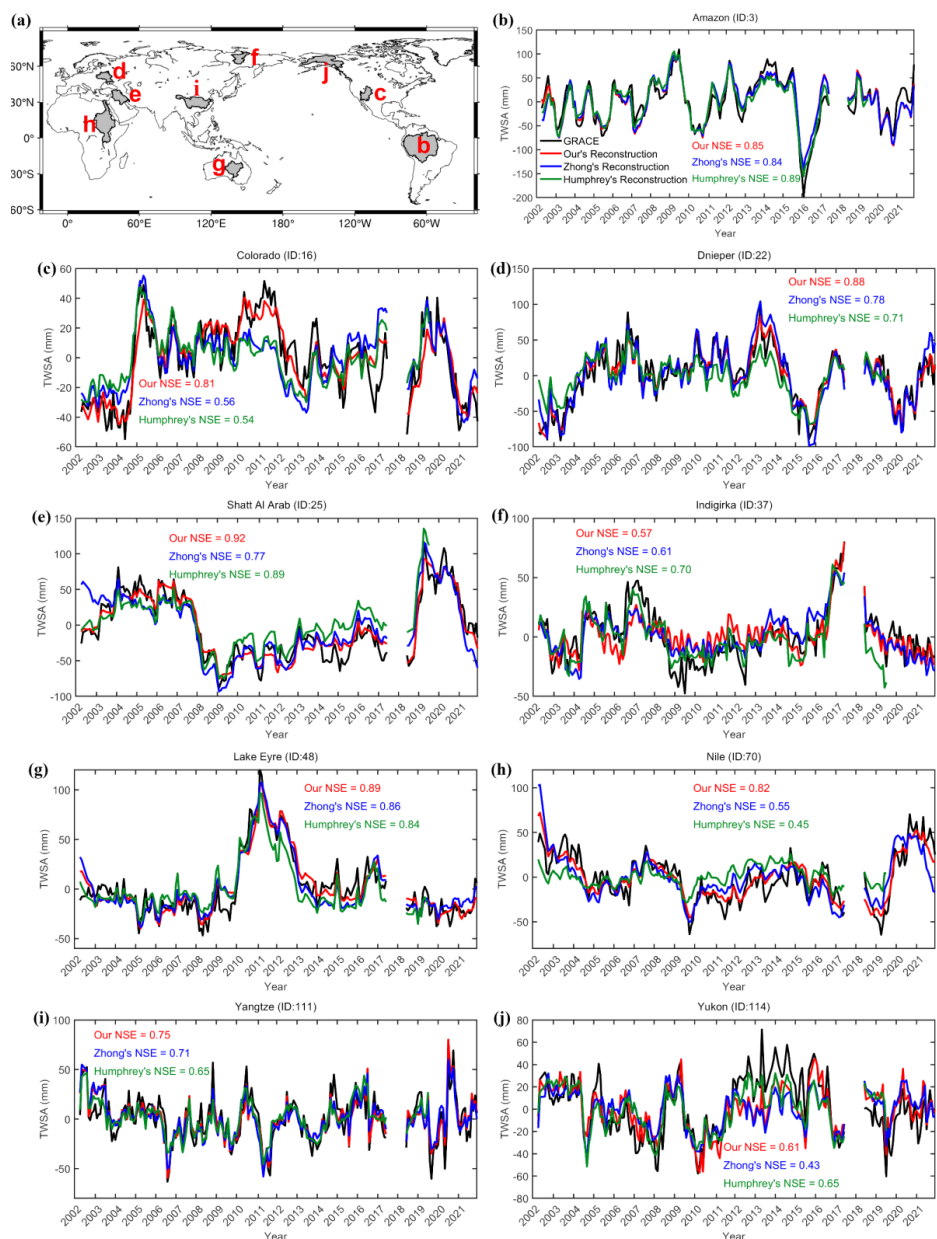


414 floods and droughts, thereby significantly altering regional water balance (Chen et al., 2022). In the
415 Amazon Basin, the La Niña event of 2009 markedly increased regional precipitation (Chen et al.,
416 2010), while the strong El Niño of 2015–2016 led to severe drought conditions (Tian et al., 2021).
417 The proposed reconstruction model successfully captured both the water storage peak in 2009 and
418 the pronounced depletion in 2016. In the Yangtze River Basin, the early 2010 La Niña event was
419 one of the primary drivers of drought, as it weakened the East Asian summer monsoon and caused
420 an eastward retreat of the western Pacific subtropical high, thereby reducing moisture transport and
421 triggering drought in the middle and lower reaches (Li et al., 2023; Zhang et al., 2015). The sharp
422 decline in TWSA observed by GRACE during this period was accurately reproduced by the present
423 model. In the Nile Basin, due to the slower response of TWS compared to precipitation, the
424 reduction in net precipitation caused by the 2008 La Niña event did not immediately lead to a decline
425 in TWSA. Instead, TWSA exhibited a gradual downward trend from 2008 to 2010 (Forootan et al.,
426 2019), and this phase lag was also captured by the model. During the strong La Niña of the period
427 from 2010 to 2011, northern and inland Australia experienced abnormally wet conditions. In the
428 Lake Eyre Basin, intense rainfall and widespread flooding caused a significant rise in TWSA (Chen
429 et al., 2022). The reconstructed TWSA time series in this basin is highly consistent with GRACE
430 observations.

431 In contrast to the basins discussed above, interannual anomalies in river basins such as the
432 Colorado and Shatt al-Arab are closely coupled with human water extraction. In the Colorado Basin,
433 groundwater levels experienced a brief recovery from 2009 to 2010 due to increased precipitation.
434 However, an anomalous drought event in 2012, combined with record-low snowfall in the Rocky
435 Mountains, led to a rapid decline in water storage (Castle et al., 2014). Similarly, since the onset of
436 drought in 2007, the Shatt al-Arab Basin has experienced a sharp decline in precipitation,
437 compounded by a rapid drop in upstream reservoir levels along the Euphrates River. As surface
438 water supplies became insufficient to meet demand, groundwater abstraction surged and became the
439 primary source for agricultural and domestic use, leading to a rapid depletion of groundwater storage
440 (Voss et al., 2013). In the high-latitude Indigirka Basin, winter precipitation is primarily stored in
441 solid form, with snow water equivalent (SWE) gradually accumulating throughout the frozen season
442 and then melting intensively in the following summer. GRACE effectively captured this “snow
443 accumulation–melt” process, showing a spring peak of approximately 50 mm from 2006 to 2007.
444 By contrast, the four-parameter recursive model developed in this study treats all precipitation $P(t)$
445 as an immediate input flux, which is attenuated through a memory term $(c \cdot T_z + d) \cdot TWS(t - 1)$.
446 This assumption leads to premature dissipation of the snow accumulation signal during winter,



447 resulting in significant underestimation of the seasonal peak. Meanwhile, the relatively large
448 constant memory coefficient d caused part of the residual water to be released with a delay,
449 resulting in overall higher reconstructed TWSA compared to GRACE observations from 2008 to
450 2010. Among all basins examined, this basin exhibited the poorest performance of our method
451 relative to previous models.



452

453 Figure 6: Time series of GRACE/GRACE-FO TWSA and reconstructed TWSA, both de-seasonalized and de-
 454 trended, for the nine selected river basins (b-j) from 2002 to 2021. The global distribution of the nine selected river
 455 basins (a).

456



457 **5 Discussions**

458 **5.1 Sensitivity Analysis of the Model**

459 **5.1.1 Sensitivity to Temporal Resolution**

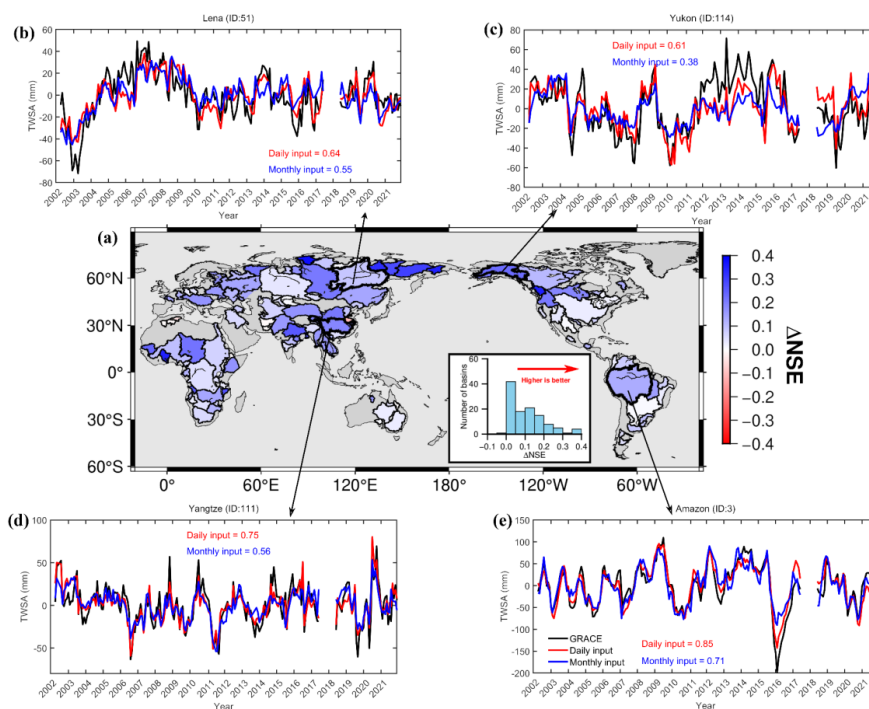
460 We first evaluated the impact of the temporal resolution of meteorological forcing data on
461 reconstruction performance, specifically whether daily forcing provides additional benefit compared
462 to monthly forcing. To this end, all 116 basins were recalibrated using both daily and monthly ERA5-
463 Land precipitation and temperature. The monthly forcing datasets were aggregated from daily values:
464 precipitation was summed to monthly totals, and temperature was averaged over each month. The
465 deseasonalized and detrended TWSA reconstructions were then compared on a monthly basis, and
466 NSE was computed for each case. The difference between the two forcing schemes was quantified
467 as $\Delta NSE = NSE_{Daily} - NSE_{Monthly}$, with its spatial distribution shown in Fig. 7a. Positive values
468 indicate better performance under daily forcing.

469 The results show that 108 out of 116 basins (approximately 95%) exhibit positive ΔNSE
470 values, suggesting that daily forcing generally outperforms monthly forcing. The most significant
471 improvements were observed in high-latitude permafrost–glacier transition zones such as Siberia
472 and Alaska. In contrast, tropical humid basins (e.g., the Paraná Basin) exhibited minimal differences
473 ($\Delta NSE \leq \pm 0.05$). Only seven basins (approximately 5%), such as the Huai River Basin, showed
474 slightly negative differences ($-0.1 < \Delta NSE < 0$), mostly located in regions with strong human
475 regulation or sparse observational data.

476 From a time series perspective, the reconstructed TWSA driven by monthly climate forcing
477 exhibits significantly lower amplitude compared to that driven by daily forcing. This is mainly due
478 to two factors: daily forcing preserves extreme precipitation events and high-frequency temperature
479 fluctuations on a day-to-day basis, allowing short-term water flux pulses to enter the recursive
480 system as sharp peaks. In contrast, monthly forcing involves pre-integrating or averaging over 30-
481 day precipitation and temperature records before inputting them into the model, which smooths out
482 extreme events and leads to underestimated amplitude in the simulations (Humphrey et al., 2016).
483 In addition, the memory coefficient calibrated at the daily time step typically ranges from $d_{day} \approx$
484 0.97 to 0.995, indicating very limited attenuation on a daily basis. When directly scaled to a
485 monthly time step, this corresponds to $d_{day}^{30} \approx 0.74$; alternatively, recalibration at the monthly scale
486 yields an equivalent memory coefficient of approximately $d_{day}^{30} \approx 0.7$ to 0.8. Both cases imply a
487 stronger low-pass filtering effect, which further dampens peak values and elevates troughs.



488 Therefore, we argue that daily forcing is essential for improving model fidelity across nearly all
 489 basins and should be considered necessary for accurate reconstruction.



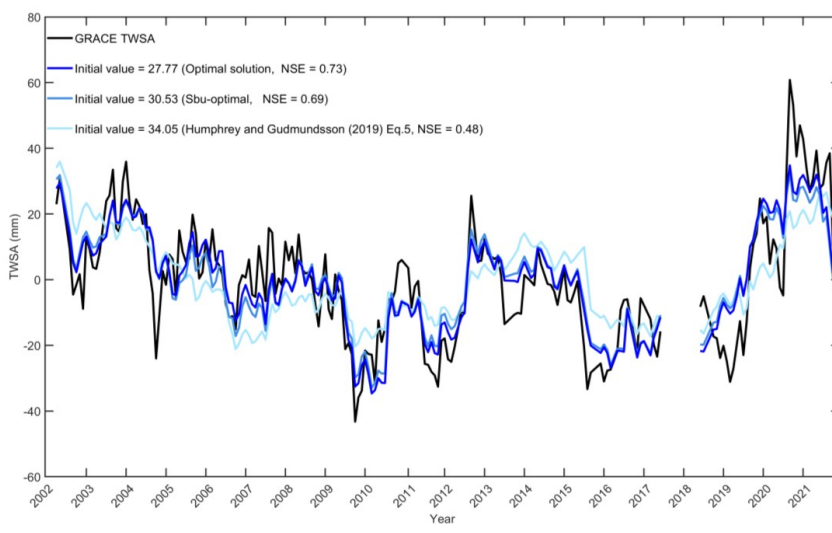
490
 491 Figure 7: Spatial distribution of the difference in NSE between TWSA reconstructions forced by daily and monthly
 492 meteorological data, with respect to GRACE JPLM from 2002 to 2021 (a). Time series of GRACE/GRACE-FO
 493 TWSA and reconstructed TWSA (de-seasonalized and de-trended) using daily and monthly meteorological data
 494 in the (b) Lena, (c) Yukon, (d) Yangtze, and (e) Amazon basins.

495 5.1.2 Sensitivity to Initial Conditions

496 This section investigates the influence of the initial terrestrial water storage, $TWS(0)$, on
 497 reconstruction performance. Humphrey and Gudmundsson (2019) demonstrated through
 498 experiments that if $TWS(0)$ is simply set to zero, the model requires a spin-up period before
 499 reaching equilibrium. To avoid discarding multiple years of data, they derived an analytical
 500 equilibrium value to serve as a uniform initialization for $TWS(0)$. However, when a basin is not in
 501 climatic equilibrium, this equilibrium-based initialization can introduce systematic bias. Since the
 502 model's memory decay coefficient ($c \cdot T_z + d$) is approximately equal to 1, such bias can persist
 503 for several years in basins with long water residence times, making the initial condition a critical
 504 factor influencing reconstruction accuracy in long-memory basins. To mitigate this bias, $TWS(0)$



505 in this study is jointly estimated along with the model parameters (a, b, c, d). Three initialization
506 strategies were compared (Fig. 8): (1) the optimal solution where $TWS(0)$ is treated as an unknown
507 and solved through least squares estimation; (2) a suboptimal solution, obtained by increasing the
508 optimal value by 10%; and (3) the equilibrium solution, derived from Eq. (5). Using the Chad Basin
509 as an example, the NSE of the equilibrium initialization was 0.48, which increased to 0.57 under the
510 suboptimal case and further improved to 0.73 under the globally optimal initialization. Therefore,
511 in this study, $TWS(0)$ is retrieved through parameter inversion for all basins, substantially
512 reducing systematic bias and enhancing reconstruction accuracy.



513
514 Figure 8: Time series of TWSA in the Chad Basin from GRACE observations and model reconstructions under
515 three different initial condition strategies. GRACE data (black) are based on the JPLM; model reconstructions are
516 obtained using (1) an optimized initialization (dark blue), (2) a sub-optimal initialization (medium blue), and (3)
517 an equilibrium initialization following Eq. (5) of Humphrey and Gudmundsson (2019) (light blue).

518 5.2 Discussion of Parameter Sensitivity

519 5.2.1 Parameter a

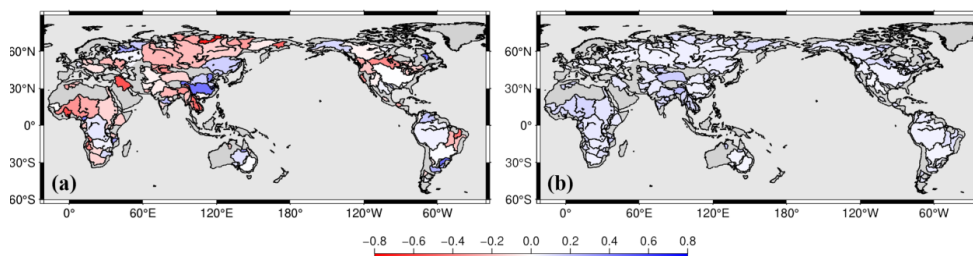
520 Figure 9 illustrates the global distribution of parameter a and its associated uncertainty. The
521 spatial pattern of parameter a exhibits pronounced contrasts across different climatic zones. In
522 high-latitude cold regions, liquid runoff is nearly absent during winter, and when temperatures rise
523 above 0°C in summer, rapid snowmelt occurs. However, the presence of permafrost and surface ice
524 layers greatly reduces infiltration capacity, causing meltwater to be discharged primarily as surface
525 runoff rather than being retained in terrestrial water storage. As a result, the inversion yields $a < 0$,



526 indicating that warming diminishes the efficiency of precipitation conversion into TWS.

527 In low-latitude arid and semi-arid regions, the annual mean ET/P ratio is high (Fig. S5), and
528 evapotranspiration plays a dominant role in the water balance. As temperature increases, potential
529 evapotranspiration intensifies, leading to greater atmospheric loss of precipitation before infiltration,
530 which similarly results in $a < 0$. In contrast, the Yangtze River Basin exhibits a positive response
531 ($a > 0$), as warming coincides with the wet season and ET/P remains relatively low (Fig. S5). Under
532 these conditions, soil and vegetation can effectively retain and infiltrate rainfall, thereby enhancing
533 the conversion of precipitation into terrestrial water storage. Similarly, in the Yellow River Basin,
534 large-scale ecological restoration projects in recent years have substantially improved vegetation
535 cover, soil structure, and infiltration conditions, resulting in significant increases in both surface and
536 groundwater storage (Feng et al., 2025). Consequently, when temperatures rise and
537 evapotranspiration intensifies, the enhanced soil water retention and groundwater recharge are
538 sufficient to offset the additional evaporative losses. As a result, the model likewise yields a positive
539 response with $a > 0$.

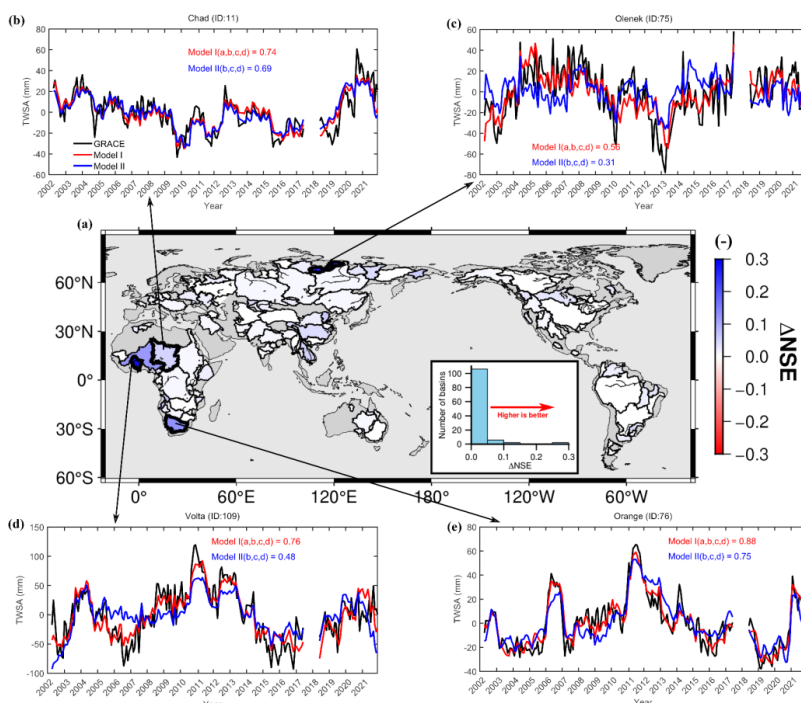
540 Figure 10a compares the full four-parameter model with a reduced three-parameter version in
541 which the temperature and precipitation coupling term (i.e., parameter a) is excluded. The global
542 distribution of ΔNSE indicates that, on average, the contribution of parameter a is limited.
543 However, under specific hydroclimatic conditions, incorporating parameter a can lead to
544 improvements in model performance with $\Delta NSE > 0.1$. Notable improvements are concentrated in
545 high-latitude snow-dominated basins, such as the Olenek River, and in certain arid regions with high
546 evapotranspiration, such as the Volta Basin. For the remaining 112 basins, ΔNSE values are below
547 0.1, suggesting no statistically significant difference. From a time series perspective, excluding
548 parameter a in the Volta Basin leads to an overestimation of summer peaks during 2005–2006 and
549 an underestimation during 2009–2012. In regions with high temperatures, removing parameter a
550 impairs the model's ability to capture interannual peak and trough variability.



551



552 Figure 9: Spatial distribution of parameter a (a), and parameter a errors (b) across global 116 river basins.
553 Parameters calibrated by monthly TWSA from JPLM based on ERA5-Land P and temperature from 2002 to 2021.
554 Uncertainty estimation of parameters based on Monte Carlo simulations using precipitation and temperature errors
555 across each basin. Precipitation errors were derived from the standard deviation between ERA5-Land and MSWEP
556 datasets. Temperature errors were derived from the standard deviation between ERA5-Land and GLDAS GLSM
557 datasets.



558

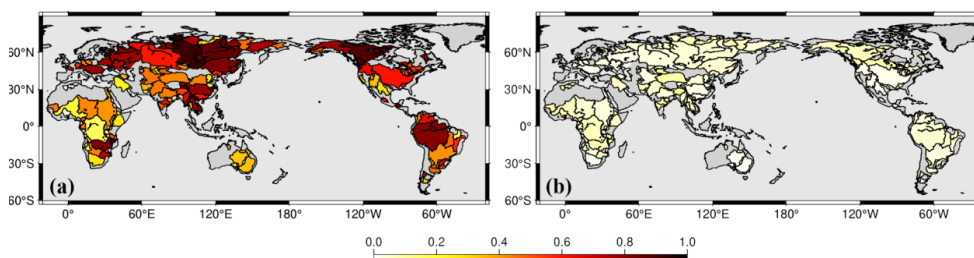
559 Figure 10: Spatial distribution of the NSE difference between TWSA reconstructions from a four-parameter and a
560 three-parameter (excluding parameter a) daily recursive model with respect to JPLM across 116 global river
561 basins during 2002–2021 (a). Time series of GRACE/GRACE-FO TWSA and reconstructed TWSA (de-
562 seasonalized and de-trended) in the (b) Chad, (c) Olenek, (d) Volta, and (e) Orange basins.

563 5.2.2 Parameter b

564 Figure 11 shows the global distribution of parameter b and its associated uncertainty. As illustrated,
565 the spatial pattern of b is consistent with the findings of Zhong et al. (2025): high-latitude regions,
566 where winter snow accounts for a substantial portion of total precipitation, require larger values of
567 parameter b to compensate for the temporary storage effect of snow accumulation. In arid and
568 semi-arid basins across the mid- to low latitudes, ET/P ratios are generally high (Fig. S5). As



569 evapotranspiration dominates the depletion of shallow soil moisture, a substantial portion of
570 precipitation is lost to the atmosphere before it can infiltrate or recharge groundwater, resulting in
571 relatively low values of parameter b . In contrast, humid basins at similar latitudes exhibit lower
572 ET/P ratios, where only a small fraction of precipitation is consumed by evapotranspiration.
573 Consequently, a greater share of precipitation contributes to terrestrial water storage, leading to
574 higher b values.



575

576 Figure 11: Spatial distribution of parameter b (a), and parameter b errors (b) across global 116 river basins.
577 Parameters calibrated by monthly TWSA from JPLM based on ERA5-Land P and temperature from 2002 to 2021.
578 Uncertainty estimation of parameters based on Monte Carlo simulations using precipitation and temperature errors
579 across each basin. Precipitation errors were derived from the standard deviation between ERA5-Land and MSWEP
580 datasets. Temperature errors were derived from the standard deviation between ERA5-Land and GLDAS GLSM
581 datasets.

582 5.2.2 Parameter c

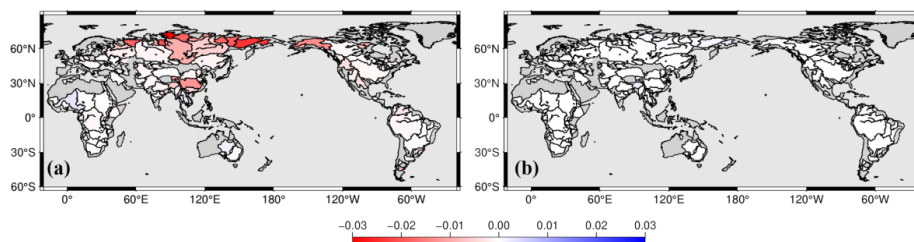
583 Figure 12 shows the global distribution of parameter c and its associated uncertainty. In high-
584 latitude basins, parameter c is predominantly negative, indicating that rising temperatures
585 substantially reduce the contemporaneous water retention rate. This pattern aligns with typical high-
586 latitude hydrological processes: winter precipitation is stored in solid form and rapidly melts during
587 spring warming, resulting in surface runoff and a sharp decline in TWS. In contrast, low-latitude
588 regions lack large-scale snow accumulation and melt processes, resulting in weaker coupling
589 between temperature and the memory term. As a result, parameter c values in these regions are
590 typically close to zero. The spatial distribution of parameter uncertainty (Fig. 12b) further shows
591 that estimation errors are relatively small in most regions, suggesting that the adopted calibration
592 approach is stable and robust across the majority of basins.

593 Figure 13 compares the full four-parameter model with a reduced three-parameter version
594 excluding parameter c . Among the 116 basins analyzed, most exhibit limited sensitivity to
595 parameter c ; however, incorporating c still yields measurable performance improvements in some
596 cases, with 11 basins showing $\Delta NSE > 0.1$. Notable improvements are concentrated in high-



597 latitude cold regions around the Arctic (e.g., Yana, Yukon, and Lena), while limited improvements
598 are found in parts of North America (e.g., Columbia, Colorado, and Rio Grande) and in certain
599 Chinese basins (e.g., Yangtze and Yellow River).

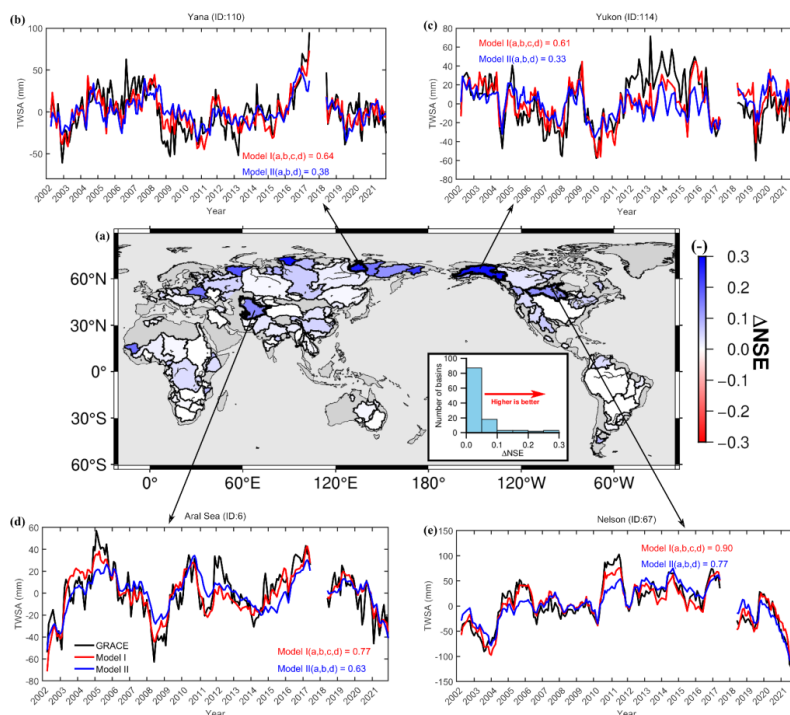
600 From a time series perspective, in the Yukon Basin, the average temperatures during the
601 snowmelt seasons of the period from 2006 to 2007 and in 2009 were markedly below normal (Fig.
602 S3). Under these conditions, the decay factor ($c \cdot T_z + d$) remained close to the baseline value d ,
603 resulting in a slower dissipation rate. Meanwhile, SWE during these years was also below the multi-
604 year average, limiting the contribution from snowmelt. GRACE observations captured a slight
605 increase in TWS during spring, followed by a continuous decline. The four-parameter model
606 successfully reproduced this slow depletion process (Fig. 13c). In contrast, the three-parameter
607 model, due to the absence of a temperature modulation term, maintains a higher retention rate under
608 the same precipitation input and consequently produces an overall overestimation in the
609 reconstructed TWS curve. Conversely, 2019 was an exceptionally warm year, with precipitation
610 anomalies remaining positive from 2017 to 2021. Rising temperatures substantially reduce ($c \cdot T_z +$
611 d), thereby accelerating the depletion of antecedent water storage. The abundant snowpack was
612 rapidly flushed during the melt season, resulting in a deeper TWS trough recorded by GRACE
613 compared to that of 2006 to 2007. The four-parameter model captured this deep trough due to the
614 dynamic weakening effect of the parameter c , whereas the three-parameter model produced a
615 shallower minimum. A similar pattern is observed in the Yana Basin: exceptionally high SWE in
616 2007 led to elevated TWS levels, while reduced snowmelt and elevated temperatures in the
617 following year (Fig. S4) triggered rapid snowmelt and a sharp decline in TWS during 2008. The
618 four-parameter model exhibits better agreement with GRACE observations, whereas the three-
619 parameter model shows excessive smoothing (Fig. 13b). These comparisons highlight the critical
620 role of the temperature modulation term c in accurately capturing TWS extremes during warm years
621 or periods of rapid snowmelt.



622



623 Figure 12: Spatial distribution of parameter c (a), and parameter c uncertainties (b) across global 116 river
 624 basins.



625
 626 Figure 13: Spatial distribution of the NSE difference between TWSA reconstructions from a four-parameter and a
 627 three-parameter (excluding parameter c) daily recursive model with respect to JPLM across 116 global river
 628 basins during 2002-2021 (a). Time series of GRACE/GRACE-FO TWSA and reconstructed TWSA (de-
 629 seasonalized and de-trended) in the (b) Yana, (c) Yukon, (d) Aral Sea, and (e) Nelson basins.

630 5.2.3 Parameter d

631 In the linear storage model, when no additional precipitation input is introduced, water
 632 depletion follows an exponential decay process. As shown in Fig. 14, when the baseline memory
 633 coefficient $d = 0.97$, and in the absence of both additional precipitation input and temperature
 634 effects, only 40% of the stored water remains after one month. In contrast, when $d = 0.99$, more
 635 than 70% of the stored water can still be retained after one month under the same condition. This
 636 indicates that the interannual variability of TWS is highly sensitive to the value of parameter d .

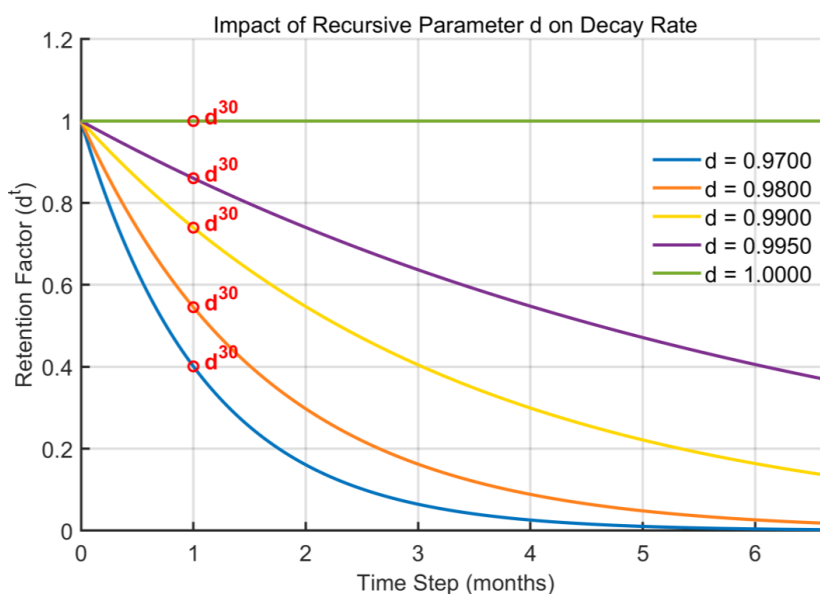
637 Figure 15 presents the global distribution of the 30-day retention factor (d^{30}) and its associated
 638 uncertainty. In high-latitude regions of the Northern Hemisphere, the widespread presence of
 639 permafrost limits the infiltration of meltwater during the spring thaw, causing most of the water to



640 be rapidly discharged as surface runoff. As a result, the calibrated baseline memory coefficient is
641 relatively low, typically ranging from 0.98 to 0.99. Although this value implies a faster daily decay
642 rate, persistent snowfall during winter months largely compensates for water loss. When
643 temperatures rise in spring, the negative value of parameter c quickly reduces the instantaneous
644 retention rate, allowing the model to effectively capture the rapid recession of water storage
645 observed by GRACE.

646 Notably, the Ob and Mackenzie River basins exhibit considerably higher water retention after
647 30 days of decay compared to other high-latitude basins (Fig. 15a). In the Ob basin, approximately
648 15% of the upstream and midstream region between the Irtysh River and the upper Ob is occupied
649 by endorheic depressions, where inflow is retained and does not contribute to the main channel (Yi
650 et al., 2023). Additionally, springtime ice jams, channel backwater, and overbank flooding further
651 prolong the average residence time of water, resulting in a higher calibrated 30-day retention
652 coefficient (d^{30}). In the Mackenzie basin, the presence of multiple large lakes leads to a highly
653 fragmented river network (Yi et al., 2023), impeding the continuous drainage of liquid water and
654 thereby extending the residence time of water within the basin.

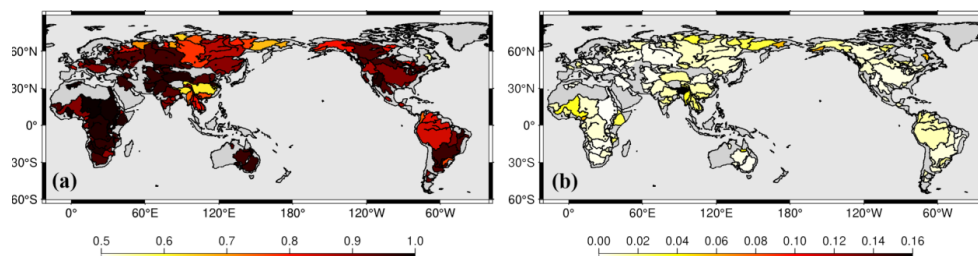
655 In contrast, tropical and subtropical basins are characterized by deep groundwater reservoirs
656 and long residence times, with no seasonal clearing effect from freeze and thaw processes. As a
657 result, the calibration favors higher values of parameter d (typically 0.995 to 0.998) to reproduce
658 the slow depletion of water storage over several months.



659



660 Figure 14: Comparison of the temporal evolution of the decay factor under different values of parameter d (t in
661 days).

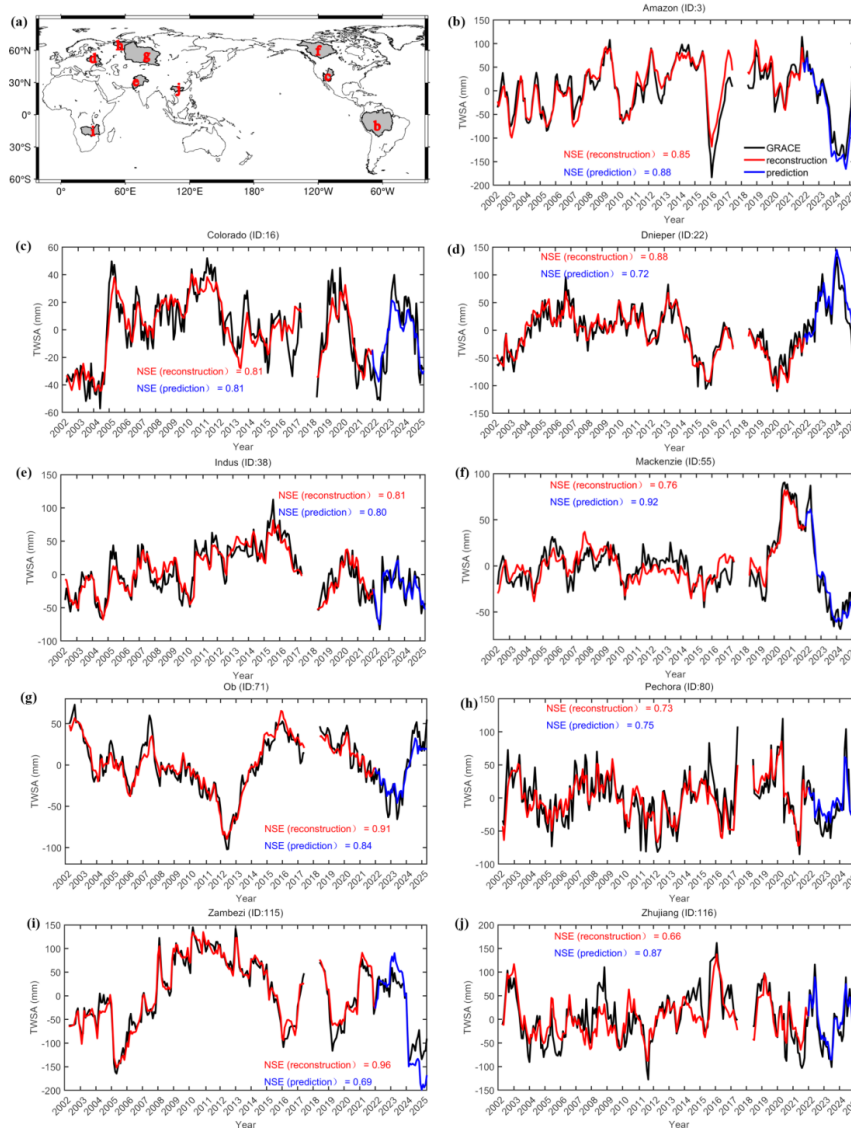


662

663 Figure 15: Spatial distribution of the 30-day retention factor d^{30} (a) and the uncertainty of parameter d^{30} (b)
664 across 116 global river basins.

665 5.3 Model Extrapolation Evaluation

666 In this study, model parameters were calibrated using GRACE data from 2002 to 2021 as the
667 training period. These parameters were then held constant to extrapolate TWSA for the period from
668 January 2022 to June 2025. To assess regional applicability, nine representative basins were selected
669 (Fig. 16), spanning high-latitude cold regions, tropical humid zones, and typical monsoon-affected
670 areas. For each basin, the predicted TWSA (blue line) was compared with the reconstructed values
671 during the training period (red line) and GRACE observations (black line). The results show that in
672 certain basins, such as the Amazon and Colorado, model performance during the extrapolation
673 period remained comparable to or even exceeded that during the training period. This indicates that
674 under these hydroclimatic conditions, the fixed-parameter model can reliably capture TWSA
675 variations driven by precipitation and temperature. For example, during the period from 2022 to
676 2024, the Amazon Basin experienced a severe extreme drought event (Fig. 16b). This event was
677 primarily driven by two factors: (1) a significant reduction in precipitation due to enhanced
678 atmospheric stability and suppressed convection; and (2) a persistent increase in atmospheric
679 evaporative demand under extreme high-temperature conditions (Fernández-Alvarez et al., 2025).
680 In some other basins, however, the predicted NSE dropped substantially. This decline may be
681 attributed to the limitations imposed by parameter nonstationarity and errors in the forcing data.
682 These results suggest that when only precipitation and temperature forecasts are available, the
683 proposed recursive model can be directly applied for estimating TWS changes during missing
684 periods or into the future. Nevertheless, its applicability varies with hydroclimatic conditions, and
685 for regions requiring high prediction accuracy, periodic parameter updates or the inclusion of
686 additional forcing information may still be necessary.



687

688 Figure 16: Time series of GRACE TWSA (black), reconstructed TWSA (red), and four-parameter climate-driven
689 forecasts (blue) from January 2022 to May 2025 in nine basins (b-j). The global distribution of the nine selected
690 river basins (a).

691 5.4 Limitations of the study

692 This approach relies on external precipitation and temperature forecasts for predicting future
693 TWSA. In regions where precipitation and temperature forecasts are relatively accurate, the model
694 is capable of producing reliable climate-driven TWSA predictions. Conversely, uncertainties in the



695 forcing data can significantly affect the reconstruction results. Therefore, both the applicability and
696 the upper limit of prediction accuracy are constrained by the quality of the forcing inputs. In addition,
697 the current model is designed to simulate deseasonalized and detrended TWSA only, and is not
698 capable of independently reproducing the full seasonal component or long-term trend.

699 In permafrost- and glacier-dominated basins, model performance is further limited. Taking the
700 Yukon Basin as an example (Fig. 6a), during the period from 2011 to 2014, the average temperatures
701 during the snowmelt seasons were significantly lower than normal for three consecutive years, while
702 annual precipitation slightly exceeded the long-term mean (Fig. S3). GRACE observations show
703 that TWSA remained at a consistently high level during this period, whereas our reconstruction
704 results are notably lower than those from GRACE. The primary source of error is likely associated
705 with the sub-daily freezing and thawing cycles within the snowpack, which is not explicitly
706 represented in the model. Meltwater generated during daytime warming is treated as immediate
707 runoff and removed from the system, while at night, when temperatures drop below 0 °C, a portion
708 of this water refreezes and is retained in the snowpack. Since the model does not incorporate this
709 refreezing into the subsequent day's initial storage, it systematically underestimates the net
710 accumulation within the snow layer. As a result, the peak in winter and spring is dampened, and the
711 overall reconstructed TWSA is biased low.

712

713 **6 Conclusions**

714 Building upon the classical linear water storage framework, this study introduces coupled
715 temperature and precipitation factors to develop a four-parameter daily recursive model for
716 reconstructing climate-driven TWSA at a $0.5^\circ \times 0.5^\circ$ spatial resolution over global land areas
717 (excluding Antarctica) for the period 2002–2021. The model is calibrated against the JPL RL06 and
718 GSFC RL06v2 mascon solutions, using hourly ERA5-Land precipitation and temperature data
719 aggregated to daily time steps as forcing inputs.

720 By treating $TWS(0)$ as an additional parameter to be estimated jointly with the other model
721 parameters, the influence of initial condition errors is substantially reduced, leading to improved
722 reconstruction accuracy. Independent calibrations conducted for 116 major river basins demonstrate
723 that the model parameters are more stable compared to existing approaches, while the reduced
724 number of calibration iterations significantly enhances computational efficiency. At the gridded
725 scale, the reconstruction closely aligns with GRACE/GRACE-FO mascon observations, with 62%
726 of grid cells achieving $NSE > 0.5$ for JPL-REC and 53% for GSFC-REC. A sensitivity analysis



727 further clarifies the physical interpretation of the four model parameters and their respective roles
728 in governing hydrological processes.

729 Comparison with existing statistical products demonstrates that the proposed model performs
730 well across multiple spatial scales. At the basin scale, reconstructed TWSA results were compared
731 with those from Zhong-REC. Among the 116 global river basins examined, 84 achieved a NSE
732 greater than 0.7 using the proposed model, whereas only 59 basins (51%) exceeded this threshold
733 with Zhong-REC. In most basins, the model yields improved performance, with the most substantial
734 gains observed in arid and semi-arid regions. At the gridded scale, the reconstructed results were
735 also compared with those from the Humphrey's model. After subtracting the Humphrey-JPL-REC
736 results from the JPL-REC reconstruction, 63% of the grid cells have ΔNSE values greater than zero,
737 indicating an overall improvement in model performance. The most pronounced improvements are
738 observed across the Arabian Peninsula and large parts of Africa.

739 In summary, this study develops a climate-driven model of global TWS variability at the
740 interannual scale, based on a simple four-parameter linear response framework that relies solely on
741 precipitation and temperature as inputs. This study introduces optimization strategies to improve
742 both computational efficiency and reconstruction accuracy. The method can be further extended to
743 incorporate additional factors such as wind speed, radiation, and topography, or to adopt nonlinear
744 relationships using machine learning approaches. However, the simplicity and high computational
745 efficiency demonstrated by the proposed framework greatly enhance its applicability and
746 interpretability. Future research will focus on simulating the seasonal and long-term trends of water
747 storage and ultimately aim to separate and quantify the relative impacts of climatic factors and
748 human activities on water resources across multiple temporal scales.

749

750 **Competing interests**

751 The authors declare that they have no known competing financial interests or personal
752 relationships that could have appeared to influence the work reported in this paper.

753

754 **Author contribution**

755 P.X. conducted the data curation, formal analysis, and investigation; developed the model and
756 software; and prepared the original manuscript draft. S.Y. conceptualized the study, acquired the



757 funding, and supervised the research. Both authors contributed to the methodology and participated
758 in the review and editing of the manuscript.

759 **Acknowledgements**

760 This research is funded by the National Natural Science Foundation of China (42374103,
761 E214040201), the University of Chinese Academy of Sciences Research Start-up Grant
762 (E3ER0402A2, 110400M003).

763

764 **Data availability**

765 The authors are grateful to the NASA Goddard Space Flight Center
766 (<https://earth.gsfc.nasa.gov/geo/data/grace-mascons>), and the Jet Propulsion Laboratory
767 (https://podaac.jpl.nasa.gov/dataset/TELLUS_GRAC-GRFO_MASCON_CRI_GRID_RL06.1_V3)
768 for providing the GRACE mascon solutions. The authors thank Zhong et al. (2025) for providing
769 publicly available datasets and source code that supported the reconstruction of terrestrial water
770 storage anomalies, which are accessible from <https://doi.org/10.1038/s43247-024-01967-7>. The
771 authors also are grateful for the water storage reconstruction dataset provided by Humphrey and
772 Gudmundsson (2019) (<https://doi.org/10.6084/m9.figshare.7670849>). ERA5-Land precipitation,
773 temperature and evapotranspiration datasets are provided by [https://doi.org/10.24381/cds.e2161bac](https://doi.org/10.24381/cds.e2161bac63)
774 63(last access: 31 July 2025). MSWEP precipitation can be publicly obtained from [http://](http://www.gloh2o.org/mswep/65)
775 www.gloh2o.org/mswep/65(last access: 31 July 2025). GLDAS-GLSM data can be publicly
776 obtained from <https://disc.gsfc.nasa.gov/datasets> (last access: 31 July 2025). The boundary of global
777 river basins is available at [https://www.bafg.de/SharedDocs/ExterneLinks/GRDC/mrb_shp_zip.](https://www.bafg.de/SharedDocs/ExterneLinks/GRDC/mrb_shp_zip.html62)
778 [html62](https://www.bafg.de/SharedDocs/ExterneLinks/GRDC/mrb_shp_zip.html62) (last access: 31 July2025). Aridity index can be publicly obtained from
779 <https://doi.org/10.6084/m9.figshare.7504448.v451> (last access: 31 July2025).

780

781 **References**

782 Abbott, B. W., Bishop, K., Zarnetske, J. P., Minaudo, C., Chapin, F. S., Krause, S., Hannah, D.
783 M., Conner, L., Ellison, D., Godsey, S. E., Plont, S., Marçais, J., Kolbe, T., Huebner, A., Frei, R. J.,
784 Hampton, T., Gu, S., Buhman, M., Sara Sayedi, S., Ursache, O., Chapin, M., Henderson, K. D., and
785 Pinay, G.: Human domination of the global water cycle absent from depictions and perceptions, *Nat.*
786 *Geosci.*, 12, 533-540, 10.1038/s41561-019-0374-y, 2019.



- 787 An, L., Wang, J., Huang, J., Pokhrel, Y., Hugonnet, R., Wada, Y., Cáceres, D., Müller Schmied,
788 H., Song, C., Berthier, E., Yu, H., and Zhang, G.: Divergent Causes of Terrestrial Water Storage
789 Decline Between Drylands and Humid Regions Globally, *Geophys. Res. Lett.*, 48, e2021GL095035,
790 <https://doi.org/10.1029/2021GL095035>, 2021.
- 791 Baldocchi, D., Falge, E., Gu, L., Olson, R., Hollinger, D., Running, S., Anthoni, P., Bernhofer,
792 C., Davis, K., and Evans, R.: FLUXNET: A new tool to study the temporal and spatial variability of
793 ecosystem-scale carbon dioxide, water vapor, and energy flux densities, *Bull. Am. Meteorol. Soc.*,
794 82, 2415-2434, 2001.
- 795 Beck, H. E., van Dijk, A. I. J. M., Levizzani, V., Schellekens, J., Miralles, D. G., Martens, B.,
796 and de Roo, A.: MSWEP: 3-hourly 0.25° global gridded precipitation (1979–2015) by merging
797 gauge, satellite, and reanalysis data, *Hydrol. Earth Syst. Sci.*, 21, 589-615, 10.5194/hess-21-589-
798 2017, 2017.
- 799 Beck, H. E., Wood, E. F., Pan, M., Fisher, C. K., Miralles, D. G., van Dijk, A. I. J. M., McVicar,
800 T. R., and Adler, R. F.: MSWEP V2 Global 3-Hourly 0.1° Precipitation: Methodology and
801 Quantitative Assessment, *Bull. Am. Meteorol. Soc.*, 100, 473-500, [https://doi.org/10.1175/BAMS-](https://doi.org/10.1175/BAMS-D-17-0138.1)
802 [D-17-0138.1](https://doi.org/10.1175/BAMS-D-17-0138.1), 2019.
- 803 Castle, S. L., Thomas, B. F., Reager, J. T., Rodell, M., Swenson, S. C., and Famiglietti, J. S.:
804 Groundwater depletion during drought threatens future water security of the Colorado River Basin,
805 *Geophys. Res. Lett.*, 41, 5904-5911, 2014.
- 806 Chen, J., Cazenave, A., Dahle, C., Llovel, W., Panet, I., Pfeffer, J., and Moreira, L.:
807 Applications and challenges of GRACE and GRACE follow-on satellite gravimetry, *Surv. Geophys.*,
808 43, 305-345, 2022.
- 809 Chen, J. L., Wilson, C. R., and Tapley, B. D.: The 2009 exceptional Amazon flood and
810 interannual terrestrial water storage change observed by GRACE, *Water Resour. Res.*, 46, 2010.
- 811 Chen, M., Shi, W., Xie, P., Silva, V. B., Kousky, V. E., Wayne Higgins, R., and Janowiak, J. E.:
812 Assessing objective techniques for gauge - based analyses of global daily precipitation, *J. Geophys.*
813 *Res.-Atmos.*, 113, 2008.
- 814 Crochemore, L., Isberg, K., Pimentel, R., Pineda, L., Hasan, A., and Arheimer, B.: Lessons
815 learnt from checking the quality of openly accessible river flow data worldwide, *Hydrol. Sci. J.*, 65,
816 699-711, 2020.
- 817 Duan, A., Zhong, Y., Xu, G., Yang, K., Tian, B., Wu, Y., Bai, H., and Hu, E.: Quantifying the
818 2022 extreme drought in the Yangtze River Basin using GRACE-FO, *J. Hydrol.*, 630, 130680, 2024.
- 819 Fan, C., Song, C., Liu, K., Ke, L., Xue, B., Chen, T., Fu, C., and Cheng, J.: Century - scale
820 reconstruction of water storage changes of the largest lake in the inner Mongolia plateau using a
821 machine learning approach, *Water Resour. Res.*, 57, e2020WR028831, 2021.
- 822 Fekete, B. M., Looser, U., Pietroniro, A., and Robarts, R. D.: Rationale for monitoring
823 discharge on the ground, *J. Hydrometeorol.*, 13, 1977-1986, 2012.
- 824 Feng, J., Li, B., Song, J., Tang, B., Nyein, M. M., and Tani, B. P.: Spatiotemporal Variations of
825 Terrestrial Water Storage and Driving Factors in the Water Towers of Northwest China Based on
826 GRACE and Multi-Source Data Sets, *Water Resour. Res.*, 61, e2024WR039490,
827 <https://doi.org/10.1029/2024WR039490>, 2025.
- 828 Fernández-Alvarez, J. C., Nieto, R., Vicente-Serrano, S. M., Carvalho, D., and Gimeno, L.:
829 Moisture and temperature sources were key drivers of the anomalies for the record-breaking of 2023
830 Amazon drought, *Commun. Earth Environ.*, 6, 801, 10.1038/s43247-025-02771-7, 2025.
- 831 Forootan, E., Khaki, M., Schumacher, M., Wulfmeyer, V., Mehrnegar, N., van Dijk, A. I.,
832 Brocca, L., Farzaneh, S., Akinluyi, F., and Ramillien, G.: Understanding the global hydrological
833 droughts of 2003–2016 and their relationships with teleconnections, *Sci. Total Environ.*, 650, 2587-
834 2604, 2019.
- 835 Humphrey, V. and Gudmundsson, L.: GRACE-REC: a reconstruction of climate-driven water



- 836 storage changes over the last century, *Earth Syst. Sci. Data*, 11, 1153-1170, 10.5194/essd-11-1153-
837 2019, 2019.
- 838 Humphrey, V., Gudmundsson, L., and Seneviratne, S. I.: Assessing Global Water Storage
839 Variability from GRACE: Trends, Seasonal Cycle, Subseasonal Anomalies and Extremes, *Surv.*
840 *Geophys.*, 37, 357-395, 10.1007/s10712-016-9367-1, 2016.
- 841 Humphrey, V., Rodell, M., and Eicker, A.: Using Satellite-Based Terrestrial Water Storage Data:
842 A Review, *Surv. Geophys.*, 44, 1489-1517, 10.1007/s10712-022-09754-9, 2023.
- 843 Lan, Z. and Wenke, S.: Progress and prospect of GRACE Mascon product and its application,
844 *Reviews of Geophysics and Planetary Physics*, 53, 35-52, 2022.
- 845 Laudon, H., Spence, C., Buttle, J., Carey, S. K., McDonnell, J. J., McNamara, J. P., Soulsby,
846 C., and Tetzlaff, D.: Save northern high-latitude catchments, *Nat. Geosci.*, 10, 324-325, 2017.
- 847 Li, B., Rodell, M., Kumar, S., Beaudoin, H. K., Getirana, A., Zaitchik, B. F., de Goncalves, L.
848 G., Cossetin, C., Bhanja, S., Mukherjee, A., Tian, S., Tangdamrongsub, N., Long, D., Nanteza, J.,
849 Lee, J., Policelli, F., Goni, I. B., Daira, D., Bila, M., de Lannoy, G., Mocko, D., Steele-Dunne, S. C.,
850 Save, H., and Bettadpur, S.: Global GRACE Data Assimilation for Groundwater and Drought
851 Monitoring: Advances and Challenges, *Water Resour. Res.*, 55, 7564-7586,
852 <https://doi.org/10.1029/2018WR024618>, 2019.
- 853 Li, F., Kusche, J., Chao, N., Wang, Z., and Löcher, A.: Long - term (1979 - present) total water
854 storage anomalies over the global land derived by reconstructing GRACE data, *Geophys. Res. Lett.*,
855 48, e2021GL093492, 2021.
- 856 Li, F., Kusche, J., Rietbroek, R., Wang, Z., Forootan, E., Schulze, K., and Lück, C.: Comparison
857 of data - driven techniques to reconstruct (1992 - 2002) and predict (2017 - 2018) GRACE - like
858 gridded total water storage changes using climate inputs, *Water Resour. Res.*, 56, e2019WR026551,
859 2020.
- 860 Li, X., Jin, T., Liu, B., Chao, N., Li, F., and Cai, Z.: The Influence of ENSO on the Long -
861 Term Water Storage Anomalies in the Middle - Lower Reaches of the Yangtze River Basin:
862 Evaluation and Analysis, *Earth Space Sci.*, 10, e2023EA003007, 2023.
- 863 Liu, B., Zou, X., Yi, S., Sneeuw, N., Cai, J., and Li, J.: Identifying and separating climate-and
864 human-driven water storage anomalies using GRACE satellite data, *Remote Sens. Environ.*, 263,
865 112559, 2021.
- 866 Liu, B., Zou, X., Yi, S., Sneeuw, N., Li, J., and Cai, J.: Reconstructing GRACE-like time series
867 of high mountain glacier mass anomalies, *Remote Sens. Environ.*, 280, 113177, 2022.
- 868 Liu, X., Feng, X., Ciais, P., and Fu, B.: Widespread decline in terrestrial water storage and its
869 link to teleconnections across Asia and eastern Europe, *Hydrol. Earth Syst. Sci.*, 24, 3663-3676,
870 10.5194/hess-24-3663-2020, 2020.
- 871 Long, D., Longuevergne, L., and Scanlon, B. R.: Global analysis of approaches for deriving
872 total water storage changes from GRACE satellites, *Water Resour. Res.*, 51, 2574-2594, 2015.
- 873 Long, D., Shen, Y., Sun, A., Hong, Y., Longuevergne, L., Yang, Y., Li, B., and Chen, L.:
874 Drought and flood monitoring for a large karst plateau in Southwest China using extended GRACE
875 data, *Remote Sens. Environ.*, 155, 145-160, 2014.
- 876 Loomis, B., Luthcke, S., and Sabaka, T.: Regularization and error characterization of GRACE
877 mascons, *Journal of geodesy*, 93, 1381-1398, 2019.
- 878 Ma, N., Zhang, Y., and Szilagyi, J.: Water-balance-based evapotranspiration for 56 large river
879 basins: A benchmarking dataset for global terrestrial evapotranspiration modeling, *J. Hydrol.*, 630,
880 130607, 2024.
- 881 Muñoz-Sabater, J., Dutra, E., Agustí-Panareda, A., Albergel, C., Arduini, G., Balsamo, G.,
882 Boussetta, S., Choulga, M., Harrigan, S., and Hersbach, H.: ERA5-Land: A state-of-the-art global
883 reanalysis dataset for land applications, *Earth Syst. Sci. Data*, 13, 4349-4383, 2021.
- 884 Muñoz Sabater, J.: ERA5-Land hourly data from 1981 to present, Copernicus climate change



- 885 service (C3S) climate data store (CDS), 10, 2019.
- 886 Ni, S., Chen, J., Wilson, C. R., Li, J., Hu, X., and Fu, R.: Global Terrestrial Water Storage
887 Changes and Connections to ENSO Events, *Surv. Geophys.*, 39, 1-22, 10.1007/s10712-017-9421-7,
888 2018.
- 889 Palazzoli, I., Ceola, S., and Gentine, P.: GR Ai CE: reconstructing terrestrial water storage
890 anomalies with recurrent neural networks, *Sci. Data*, 12, 146, 2025.
- 891 Pastorello, G., Trotta, C., Canfora, E., Chu, H., Christianson, D., Cheah, Y.-W., Poindexter, C.,
892 Chen, J., Elbashandy, A., and Humphrey, M.: The FLUXNET2015 dataset and the ONEFlux
893 processing pipeline for eddy covariance data, *Sci. Data*, 7, 225, 2020.
- 894 Riegger, J. and Tourian, M. J.: Characterization of runoff - storage relationships by satellite
895 gravimetry and remote sensing, *Water Resour. Res.*, 50, 3444-3466, 2014.
- 896 Rodell, M., Velicogna, I., and Famiglietti, J. S.: Satellite-based estimates of groundwater
897 depletion in India, *Nature*, 460, 999-1002, 2009.
- 898 Rodell, M., Famiglietti, J. S., Wiese, D. N., Reager, J., Beaulieu, H. K., Landerer, F. W., and
899 Lo, M.-H.: Emerging trends in global freshwater availability, *Nature*, 557, 651-659, 2018.
- 900 Sun, A. Y., Scanlon, B. R., Save, H., and Rateb, A.: Reconstruction of GRACE total water
901 storage through automated machine learning, *Water Resour. Res.*, 57, e2020WR028666, 2021.
- 902 Sun, Z., Long, D., Yang, W., Li, X., and Pan, Y.: Reconstruction of GRACE data on changes in
903 total water storage over the global land surface and 60 basins, *Water Resour. Res.*, 56,
904 e2019WR026250, 2020.
- 905 Tapley, B. D., Watkins, M. M., Flechtner, F., Reigber, C., Bettadpur, S., Rodell, M., Sasgen, I.,
906 Famiglietti, J. S., Landerer, F. W., and Chambers, D. P.: Contributions of GRACE to understanding
907 climate change, *Nature climate change*, 9, 358-369, 2019.
- 908 Tian, K., Wang, Z., Li, F., Gao, Y., Xiao, Y., and Liu, C.: Drought Events over the Amazon
909 River Basin (1993–2019) as Detected by the Climate-Driven Total Water Storage Change, *Remote
910 Sens.*, 13, 1124, 2021.
- 911 Trabucco, A. and Zomer, R. J.: Global Aridity Index and Potential Evapotranspiration (ET0)
912 Climate Database v3, International Center for Tropical Agriculture (CIAT) and World Agroforestry
913 Centre (ICRAF) [dataset], 10.6084/m9.figshare.7504448.v3, 2019.
- 914 Voss, K. A., Famiglietti, J. S., Lo, M., De Linage, C., Rodell, M., and Swenson, S. C.:
915 Groundwater depletion in the Middle East from GRACE with implications for transboundary water
916 management in the Tigris - Euphrates - Western Iran region, *Water Resour. Res.*, 49, 904-914, 2013.
- 917 Wiese, D., Yuan, D., Boening, C., Landerer, F. W., and Watkins, M.: JPL GRACE and GRACE-
918 FO Mascon Ocean, Ice, and Hydrology Equivalent Water Height Coastal Resolution Improvement
919 (CRI) Filtered Release 06 Version 02, DAAC: Pasadena, CA, USA, 2019.
- 920 Xiao, C., Zhong, Y., Wu, Y., Zhang, Z., Bai, H., and Li, Z.: Flood Evolution in the Past 60 Years
921 Revealed by Reconstructed Daily Terrestrial Water Storage Anomalies in China, *Water Resour. Res.*,
922 61, e2024WR038712, <https://doi.org/10.1029/2024WR038712>, 2025.
- 923 Xu, L., Chen, N., Moradkhani, H., Zhang, X., and Hu, C.: Improving global monthly and daily
924 precipitation estimation by fusing gauge observations, remote sensing, and reanalysis data sets,
925 *Water Resour. Res.*, 56, e2019WR026444, 2020.
- 926 Yi, S., Saemian, P., Sneeuw, N., and Tourian, M. J.: Estimating runoff from pan-Arctic drainage
927 basins for 2002–2019 using an improved runoff-storage relationship, *Remote Sens. Environ.*, 298,
928 113816, 2023.
- 929 Yi, S., Sun, W., Feng, W., and Chen, J.: Anthropogenic and climate-driven water depletion in
930 Asia, *Geophys. Res. Lett.*, 43, 9061-9069, <https://doi.org/10.1002/2016GL069985>, 2016.
- 931 Yin, J., Slater, L. J., Khouakhi, A., Yu, L., Liu, P., Li, F., Pokhrel, Y., and Gentine, P.: GTWS-
932 MLrec: global terrestrial water storage reconstruction by machine learning from 1940 to present,
933 *Earth Syst. Sci. Data*, 15, 5597-5615, 2023.



- 934 Zhang, D., Zhang, Q., Werner, A. D., and Liu, X.: GRACE-based hydrological drought
935 evaluation of the Yangtze River Basin, China, *J. Hydrometeorol.*, 17, 811-828, 2016.
- 936 Zhang, J., Liesch, T., and Goldscheider, N.: Impacts of climate change and human activities on
937 global groundwater storage from 2003 to 2022, *J. Hydrol.*, 664, 134298,
938 <https://doi.org/10.1016/j.jhydrol.2025.134298>, 2025.
- 939 Zhang, Z., Chao, B., Chen, J., and Wilson, C.: Terrestrial water storage anomalies of Yangtze
940 River Basin droughts observed by GRACE and connections with ENSO, *Glob. Planet. Change*, 126,
941 35-45, 2015.
- 942 Zheng, S., Zhang, Z., Yan, H., Zhao, Y., and Li, Z.: Characterizing drought events occurred in
943 the Yangtze River Basin from 1979 to 2017 by reconstructing water storage anomalies based on
944 GRACE and meteorological data, *Sci. Total Environ.*, 868, 161755,
945 <https://doi.org/10.1016/j.scitotenv.2023.161755>, 2023.
- 946 Zhong, Y., Feng, W., Humphrey, V., and Zhong, M.: Human-Induced and Climate-Driven
947 Contributions to Water Storage Variations in the Haihe River Basin, China, *Remote Sens.*, 11, 3050,
948 2019.
- 949 Zhong, Y., Tian, B., Kim, H., Yuan, X., Liu, X., Zhu, E., Wu, Y., Wang, L., and Wang, L.: Over
950 60% precipitation transformed into terrestrial water storage in global river basins from 2002 to 2021,
951 *Commun. Earth Environ.*, 6, 53, 2025.
- 952 Zomer, R. J., Xu, J., and Trabucco, A.: Version 3 of the Global Aridity Index and Potential
953 Evapotranspiration Database, *Sci. Data*, 9, 409, [10.1038/s41597-022-01493-1](https://doi.org/10.1038/s41597-022-01493-1), 2022.
- 954